Time lapse GPR tomography to image an infiltration test in the vadose zone at the Hanford site, Washington

Final Report for Task Order 1002

William P. Clement

Center for Geophysical Investigation of the Shallow Subsurface
Boise State University
Boise, ID 83725

Technical Report BSU CGISS 2003-01
February 5, 2003

Time lapse GPR tomography to image an infiltration test in the vadose zone at the Hanford site, Washington

Final Report for Task Order 1002

William P. Clement

Center for Geophysical Investigation of the Shallow Subsurface

Boise State University

Boise, ID 83725

Abstract

To measure changes in soil moisture content of the subsurface, I collected crosshole ground penetrating radar (GPR) data. I compared the changes in the GPR response during an infiltration test conducted in June, 2001. The tomography data were acquired in May, June, and September, 2001. The experiments indicated that the electromagnetic (EM) velocity of the subsurface changed over the acquisition period. In this time-lapse experiment, changes in the EM velocity are linked to changes in the soil moisture caused by the infiltration test. I can use the tomograms to map water flow through the vadose zone. The tomography did not image the vertical clastic dike that transected the infiltration test site. However, this dike may account for slow velocities in the tomograms that cross the dike. A more careful design of the tomography part of the infiltration experiment would probably result in higher data quality and more consistent images of the soil moisture distribution.

Introduction

Understanding fluid flow in the unsaturated zone is important to determine the fate and transport of contaminants. The distribution of moisture content is vital to accurate models of

vadose zone fluid flow. A reliable and non-invasive method to adequately map the moisture content distribution in the subsurface is highly desirable. The moisture content distribution will provide better input to unsaturated zone fate and transport modeling studies and thus increase the reliability of the resulting models.

The clastic dikes are vertical features that disrupt the layering of the Pleistocene flood deposits of the Hanford formation. The dikes are sedimentary features that are most commonly seen as regular-shaped polygonal networks in the Army Loop Road area. At the Army Loop Road test site, the dikes are generally composed of multiple sub-vertical layers with an outer skin of clay with coarser infilling material. The infilling material are typically poorly to well-sorted sand, but the dikes may contain clay, silt, and gravel (Murray and Fayer, 2001; Fayer, et al., 2001). The hydraulic conductivity of the surrounding flood deposits is about 10^{-3} cm/s. The center of the dikes have an average hydraulic conductivity of 10^{-3} cm/s. The dike skin has hydraulic conductivities ranging from 10^{-7} cm/s to 10^{-4} cm/s (Murray and Fayer, 2001; Fayer, et al., 2001).

Numerous networks of clastic dikes exist throughout the Hanford site. The role these dikes play in the flow of water is poorly understood. These dikes may act as barriers to horizontal flow. They may also be vertical conduits for water into the underlying aquifer. Understanding of the hydraulic character of the dikes is critical to the design of waste facilities and the remediation of contaminated sites.

An infiltration test was conducted in late May through June of 2001 to determine the hydraulic character of the clastic dikes. As part of this study, I conducted crosshole ground penetrating radar (GPR) surveys to image the infiltrating fluid. I collected GPR data in three similar experiments in May, June, and September, 2001, reoccupying the wells at the test site. This method has been successfully applied during infiltration tests (Alumbaugh, 2002; Binley, 2001).

These experiments correspond to pre-infiltration, infiltration, and post-infiltration. Analyzing changes over time in the resulting tomograms provides information on the flow of water through the vadose zone.

Methods

Crosshole Ground Penetrating Radar Tomography

Crosshole GPR tomography is used to map two-dimensional velocity changes between two wells (figure 1). An antenna is placed in each well. One antenna is held at a constant depth.

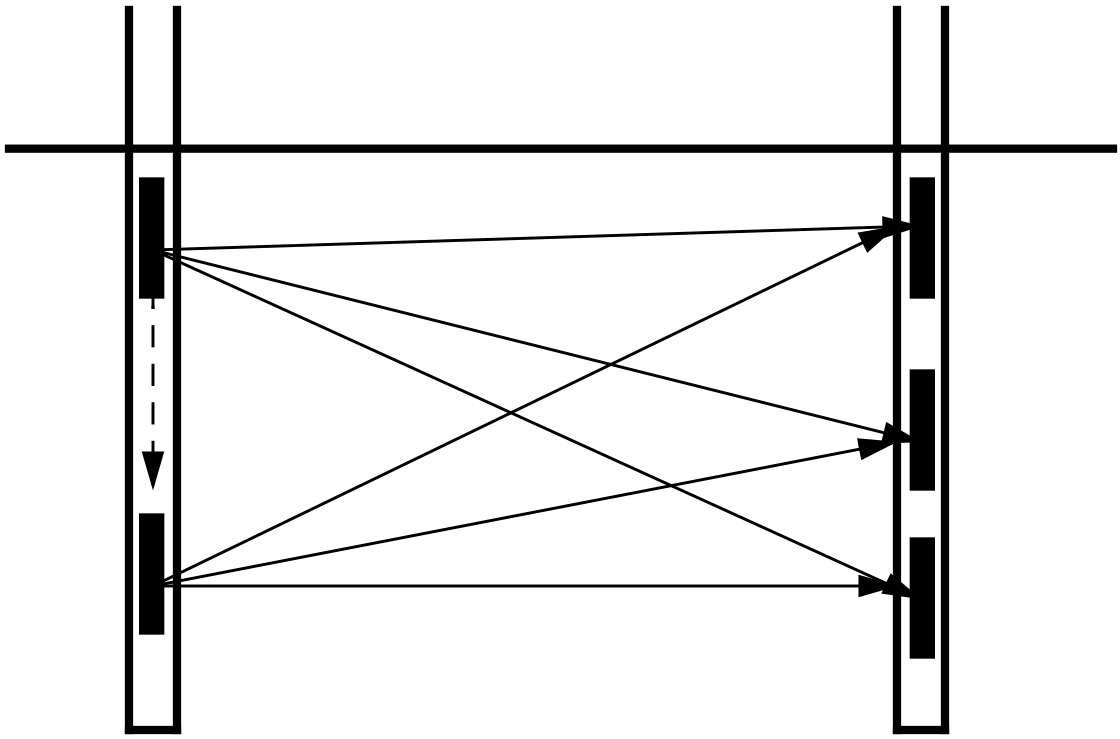

Figure 1. Geometry for crosshole tomography experiments.

The second antenna is lowered in increments down the other well, recording the arrival time of the energy transmitted by the stationary antenna. After this antenna reaches the maximum depth, usually the depth of the well, the fixed antenna is then lowered one increment. The antenna at depth is

raised to the top of the well, then lowered as before. This process is repeated until the fixed antenna has been lowered to the maximum depth. This geometry enables radar energy to repeatedly sample the space between the wells.

Tomography consists of a forward modeling and an inversion routine to derive the velocities between the two wells. In a simple, linear case, the system of equations to solve is:

$$\mathbf{Gm}=\mathbf{d}, \tag{1}$$

where **G** is a matrix, **m** are the model parameter values, and **d** is the data. In tomography, **m** is a vector of values of the inverse of velocity, or slowness. **d** is the vector of traveltimes between each source and receiver pair. **G** consists of the length of the ray in each cell in the model for all the source and receiver pairs. In the nonlinear case, **G** is also called the Jacobian matrix. Pre-multiplying each side by the inverse of **G** gives the solution:

$$\mathbf{m}=\mathbf{G}^{-1}\mathbf{d}. \tag{2}$$

In tomography, the problem is often ill-conditioned and inconsistent. In other words, some of the cells in the model are not sampled and some are oversampled. The result is that **G** is singular and an inverse does not exist. To overcome this difficulty, the equations can be reformulated into the weighted, damped, least squares solution (Menke, 1989):

$$\mathbf{m}^{\mathbf{est}} = \langle\mathbf{m}\rangle + [\mathbf{G}^{\mathbf{T}}\mathbf{W}_{\mathbf{e}}\mathbf{G} + \lambda^2 \mathbf{W}_{\mathbf{m}}]^{-1}\mathbf{G}^{\mathbf{T}}\mathbf{W}_{\mathbf{e}}[\mathbf{d}-\mathbf{G}\langle\mathbf{m}\rangle]. \tag{3}$$

Here, $\mathbf{m}^{\mathbf{est}}$ is the solution, an estimate of the true model parameters, slowness (velocity) in traveltime tomography. $\langle\mathbf{m}\rangle$ is an initial guess to the slowness (velocity) model, $\mathbf{W}_{\mathbf{e}}$ is a data weighting matrix, $\mathbf{W}_{\mathbf{m}}$ is the model weighting matrix, and λ is a parameter adjusting the relative importance

of model fit or data fit. For this analysis, $\mathbf{W_e}$ is the identity matrix and $\mathbf{W_m}$ is the regularization matrix, consisting of the finite-difference approximation to the second derivative (-1 2 -1).

To determine the velocity field, I implement a curved ray, nonlinear tomographic inversion method (Aldridge and Oldenburg, 1993). Because I am using curved rays, the path lengths are dependent on the velocity model. I linearize the problem by solving for small changes in the slowness model corresponding to traveltime differences between the observed data and the calculated values. Using more physically realistic curving rays, as opposed to the simple straight ray approximation, makes the problem more difficult to solve. However, the results should be a better estimate of the subsurface velocity distribution.

The forward model is a finite-difference approximation to the eikonal equation. The forward model algorithm computes the travel time of the first arriving energy to each node on the 2-dimensional grid. Path lengths of the ray through each cell are computed by backprojecting the ray from the receiver to the source along the gradient of the traveltime field. These path lengths are the values of the **G** or Jacobian matrix and are used by the inversion routine.

The inversion routine iteratively updates the slowness model based on equation 3 until the stopping criteria are met. The tomography routine stops when the data misfit is about the same level as the noise in the data or the number of iterations exceeds a user-defined amount. In addition, inversion uses an iterative solver, LSQR, to invert for the velocities (Paige and Saunders, 1982). The matrices in equation 3 are too large to be efficiently solved by singular value decomposition. The LSQR routine is fast, but the inverse of the matrix is not computed. Without the matrix inverse, formal estimates of resolution and covariance are not possible. The program calculates the slowness values for the plane between the two wells, then outputs the calculated, 2-D velocity distribution.

Data Acquisition

Crosshole GPR data

I visited the Army Loop Road Clastic Dike Infiltration site three times to image the change in soil moisture during the infiltration test. Table 1 lists the acquisition dates and the well pairs

Table 1: Geophysical field experiments

Survey Date	Well Pairs
May 14-20, 2001	3 to 5; 7 to 6; 3 to 7; 3 to 8; 1 to 8; 1 to 3; 1 to 7; 5 to 6; 4 to 5; 7 to 4; 2 to 3; 2 to 7
June12-14, 2001	3 to 5; 3 to 7; 7 to 6; 3 to 8; 1 to 7; 2 to 3
September 17-18, 2001	3 to 5; 3 to 7; 3 to 8; 7 to 6

used in the surveys. A cone penetrometer was used to develop and case the boreholes, labeled

CPT1 through CPT8 (figure 2). The boreholes are cased with PVC tubes, which have an inner

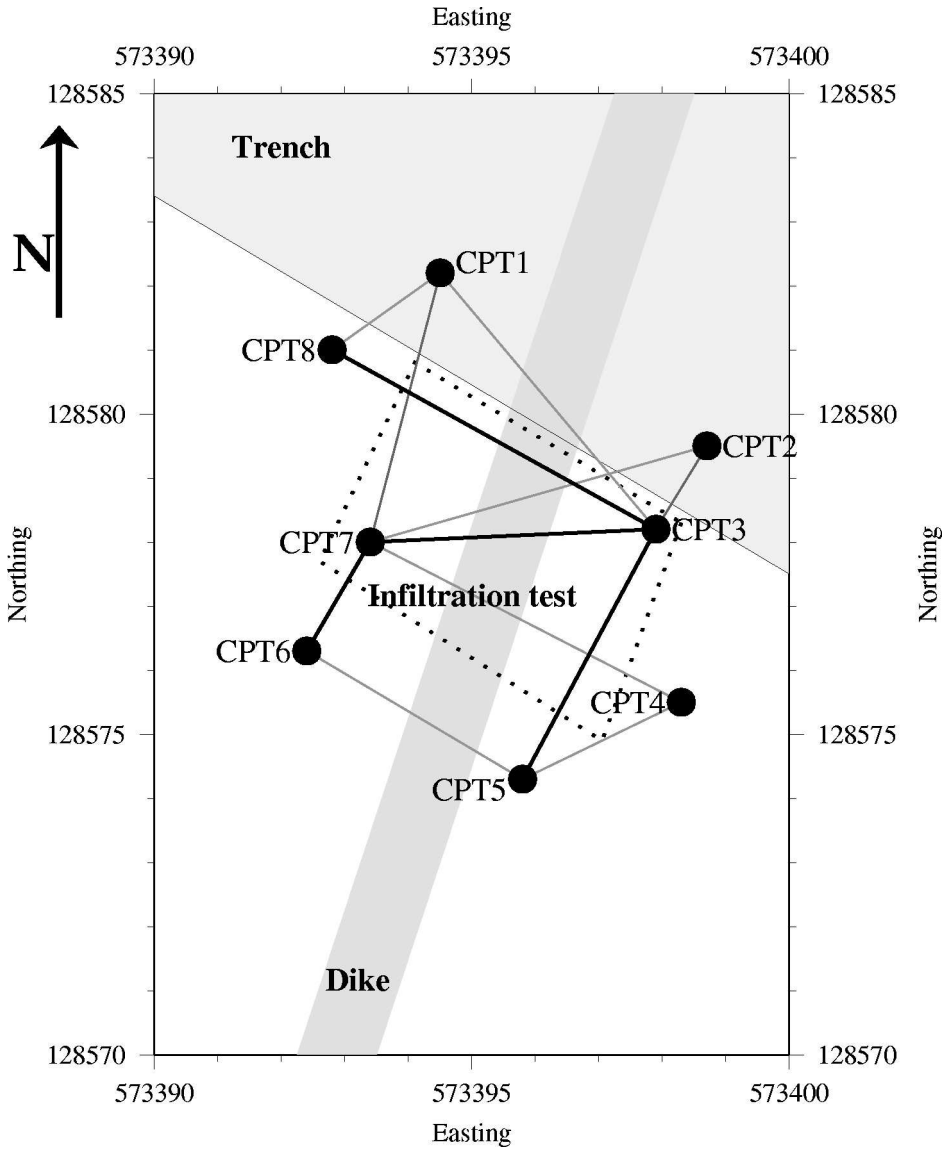

Figure 2. Layout of the infiltration experiment. Well locations are labeled. The area of infiltration is the labeled, dashed rectangle. The surface expression of the clastic dike runs south-southwest to north-northeast. The trench was excavated after the June experiments. A large, plastic and metal tent covered the infiltration area.

diameter of 2.0 inches (0.051 m). About a meter or so of this pipe extended above the land surface. Between the May and the June experiment, the top 30 to 50 cm of this extended tubing was cut off. The May data are compensated to depths corresponding to the lowered tube heights.

Also, after the May acquisition, the infiltration test area was developed. The test area was covered with “drip” hose and instrumented with TDR probes and piezometers. More significantly, a large, plastic tent with metal supports covered the infiltration area. Two wells, CPT 3 and CPT 7, were near the edges inside the tent. The low overhead at these wells made calibrating the GPR instruments difficult.

The trench was excavated between the June and September experiments. The edge of the trench was about a meter from CPT 3 and CPT 8. CPT 1 and CPT 2 were no longer accessible, although the tubes remained in place. The trenching appears not to have disturbed the sediments surrounding the other wells, especially CPT 3 and CPT 8. However, the excavation of sediment from the trench alters the material properties possibly sensed by the GPR energy. Low velocity sediments (~0.15 m/ns) removed by trenching are replaced with high velocity air (0.3 m/ns). This change in material property may introduce error or artifacts into the tomograms and may cause error in the interpretation for data recorded during the September experiment.

Figure 3 shows typical tomography shot gathers. The transmitter and receiver were low-

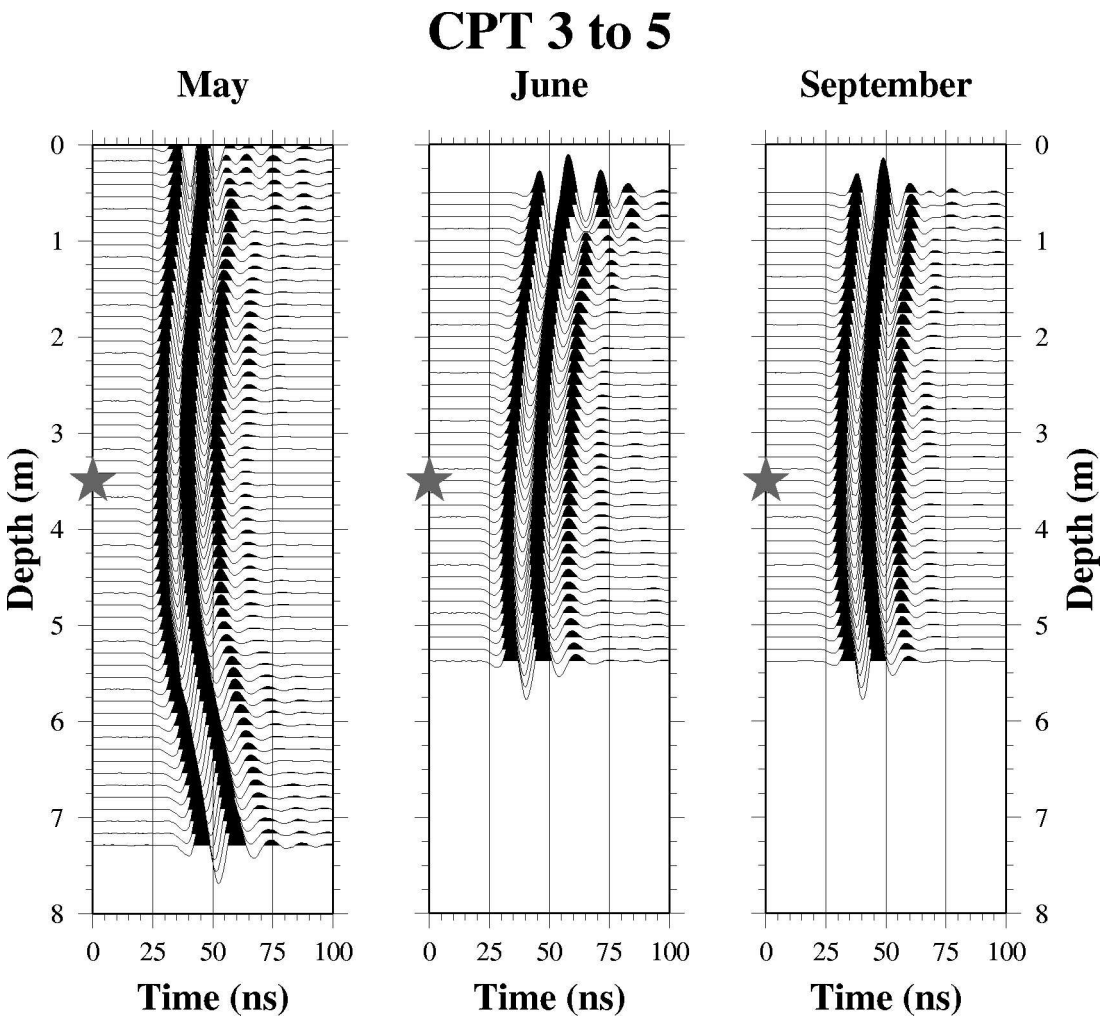

Figure 3. Tomography panels collected between wells CPT 3 and CPT 8. The star in each plot marks the depth (3.5 m) of the transmitting antenna. Traces in May start nearer the surface because the top of the tube was about 43 cm higher than the later experiments.

ered by 0.125 m increments down the boreholes. In a typical survey, the transmitter was stationed at 1.0 m at the start of the survey and was lowered to the bottom of the well. The receiver was started at 0.5 m below the top of the well casing, and lowered to the base of the well. I used 100 MHz antennas and recorded the energy using a sample interval of 0.8 ns. To improve the signal to noise ratio, the data were stacked (summed) 16 times at each position.

Several different acquisition geometries are used to ensure data quality. The radar system does not know the trigger time for the transmitted pulse. A calibration file is acquired to determine this time. At the start of acquisition between a well pair, the antennas are placed next to the wells and several traces acquired. From measurement, I know the antenna separation. The velocity of radar energy in air is 0.3 m/ns, so I can calculate the travel time between the antennas. The trigger time is the difference between the recorded arrival time on the calibration traces and the calculated time based on the antenna separation. This calibration procedure is repeated for each new well pair.

I also acquire data with the antennas lowered into the wells at equal depths. These zero-offset profiles (ZOP) usually have high quality arrival time picks. During the tomography acquisition, the lowered receiving antenna is at the same depth as the transmitting antenna for one trace. For example, with the source at 3.5 m, one trace from the gather had the receiving antenna also at 3.5 m depth. Arrival times from these pairs should be equal to the arrival times from the appropriate depth of the level runs. Thus, the ZOP data are used to correct for time drift during the duration of the tomography acquisition.

ZOPs take only a few minutes to acquire. The tomography panels often take several hours. The time base may drift due to temperature variations and battery power decay over the period of acquisition. The ZOPs, because they are acquired quickly, are not so prone to time drift. I check the difference between the level run time and the appropriate time from the tomography data and shift the entire tomography panel to align the times. (A panel is one set of travel times from one transmitter location). This procedure is repeated for all the tomography data to correct for time drift.

The first arriving travel times are picked from the crosshole GPR data. The radar sections are minimally processed to remove low frequency, “wow” energy caused by saturating the electronics. The data are also shifted by the trigger delay. The peak amplitudes near the arrival of the energy are picked automatically. These times are shifted to compensate for the delay between the onset of the energy and the peak amplitude. As described above, the time picks are carefully examined to correct for time drift errors. I pick the first arriving energy on each trace for the input data to the tomography method.

The shape of the waves in figure 3 look similar. In figure 3a, the traces extend to 7.25 m, unlike the data from June and September. In May, the transmitter was in CPT 3. In June and September, the transmitter was in CPT 5, a shallower well. The May data represents the background situation. The arrivals in figure 3a start at about 25 ns, then decrease to about 20 ns about 2.5 m below the surface. Below 5 m, the traveltimes increase to about 33 ns at the well bottom. The break in the curvature of the arrivals at about 5.7 m indicates a slow velocity zone below this depth.

In June (figure 3b), the travel times are later at all depths compared to the May data. During June, water infiltrated the ground from the infiltration test. The radar velocity in water (0.03 m/ns) is much slower velocity than the radar velocity in air (0.3 m/ns). Water replacing air in the pores will decrease the velocity of the material. The increased traveltimes in the June data correspond to slower velocities in the subsurface. In the June data, the traveltimes in the upper 3.0 m are more delayed compared to the May traveltimes. Below 3.0 m, the traveltime difference is not as large from May to June. The September data (figure 3c) are similar to the May data. The data are delayed only a nanosecond or two relative to the May data.

The data are acquired with the same acquisition parameters, so differences in the data are due to changes in the subsurface conditions. Obviously, the most significant change will be water added from the infiltration test. A travel time delay probably indicates that more water is in the pore space. The small difference between May and September indicates that the subsurface is drying out from the infiltration experiment, but that the moisture content in the ground is slightly higher than during May.

The number of travel time picks for the tomographic inversion ranges from 539 travel times for the September pair CPT 3 to CPT 7 to over 2,200 for the May pair CPT 3 to CPT 5. The data quality and the depth of the wells determined the number of picks used in the tomographic inversion. The tomography routine estimates the velocity between the well pair based on the travel time picks and the distance between the transmitter and receiver pairs. A number of parameters must be determined in order for the routine to compute the velocity field. The area between the wells is gridded into equal sized, constant slowness (velocity) cells. Each cell is 0.1 m by 0.1 m. The number of cells is computed from the acquisition geometry. To avoid edge effects, the grid is extended in four directions by 1.33 m.

In tomography problems, the solution is usually mixed-determined; some cells are not sampled and other cells are oversampled. In this case, simple inversion is not possible. Instead, the tomography routine regularizes the problem to find a solution (Aldridge and Oldenburg, 1993). The regularization scheme uses approximations to the second difference operator. This choice is often referred to as smoothing since the solution is forced to vary smoothly. A feature of the routine is that the horizontal and vertical smoothing can be weighted differently. To maintain simplicity, I used an equal weighting of 2 in each direction.

In the non-linear inversion, a starting model is necessary to avoid local minima solutions. The starting model has three layers. The first layer is 0.5 m thick with a velocity of 0.3 m/ns, representing the air accounting for the stickup height of the wells. The second layer extends to 5.5 m depth with a constant velocity of 0.14 m/ns. The last layer has a velocity of 0.12 m/ns and extends to the base of the model. This starting model is a rough approximation to the velocity structure at the clastic dike site.

Finally, the non-linear nature of the problem requires an iterative solution to the linearized system (Aldridge and Oldenburg, 1993). The routine stops iterating when the root mean square (RMS) misfit is less than 0.25 ns or the number of iterations exceeds 20. The 0.25 ns misfit value is an estimate of the error in the travel time picks. Requiring the solution to reduce the misfit more implies that the routine is seeking solutions that fit the noise in the data. Increasing the number of iterations does not significantly change the solution and may cause the solution to fit the noise in the data. Fitting the data noise will unrealistically increase the solution's complexity, providing more "information" than the data really contains.

Tomographic Analysis

Table 2 lists the average EM velocities and their range from the tomography experiment.

Table 2: Average EM velocity and range (m/ns)

CPT pairs	May	June	September
3 to 5	157.6 98.7 to 198.6	134.0 111.6 to 189.7	152.0 117.27 to 199.8
3 to 7	112.3 88.5 to 172.4	104.8 80.1to 134.5	101.6 53.6 to 182.6
3 to 8	131.0 113.1 to 143.9	133.2 117.6 to 145.9	127.7 105.2 to 151.1
7 to 6	145.0 73.5 to 200.0	137.7 58.8 to 199.9	136.0 62.0 to 199.5

The range was computed using velocity values less than 200 m/ns. Velocities faster than 200 m/ns are certainly influenced by the air at the surface. In general, the average velocities decrease from May to June, except CPT 3 - 8. From June to September, the average velocities decrease, except for CPT 3 - 5. However, the tomogram from CPT 3 - 5, September is anomalous, as seen later, and probably is inaccurate. The average velocities indicate that the subsurface velocities decreased during the tomography experiment, indicating that the ground became wetter over this time period.

CPT 3 - 7 and CPT 3 - 8 have slower average velocities; the slowest average velocities are observed in CPT 3 - 7. The average velocities are significantly slower than the other tomograms. Interestingly, these two transects cross the clastic dike whereas the other two transects are on opposite sides of the dike and do not cross the dike (figure 2). The slower average velocities in CPT 3 - 8 and CPT 3 - 7 may indicate that the clastic dike has slower velocities than the surrounding material. Looking at the geometry in Figure 2, the path through CPT 3 - 8 is perpendicular to the dike, while the path through CPT 3 - 7 is at an angle. The rays from CPT 3 - 7 travel longer in

the dike causing the slower average velocities in CPT 3 -7 than between CPT 3 - 8. The largest velocity change is in CPT 3 - 5 between May and June. This velocity decrease is probably caused by the water infiltrating during the test.

Tomograms

The tomograms are plotted with areas of low ray coverage (ray densities < 0.1) whited out to avoid interpreting areas with no information. The velocities plotted in the tomograms have the same velocity scale. In other words, the color bar is the same in all of the tomogram plots. From left to right, the three panels in each figure are from the May, June, and September surveys. The soil moisture content derived from the neutron probe data is plotted next to the appropriate CPT. I have also plotted the base line for the soil moisture content data as a vertical line. In the velocity difference plots, the first panel is the tomogram from the May experiment with the tomogram color bar (identical to the tomogram May plots). For the difference panels, the color bar indicates the velocity difference between the May tomogram and the later tomograms. Again, the color bar is the same for the velocity difference plots. I have also included the soil moisture content derived from the neutron probe data similar to the tomogram plots. However, for the velocity difference panels, I plotted the difference in soil moisture content from the May data. Thus, an increase in soil moisture from May to June would be a decrease in the velocity, or a value to the left of the base line in the soil moisture plot. The consistency of the color bars allows for direct comparison between the tomograms.

The velocity tomograms for CPT 7 - 6 show a slow velocity layer near the upper two meters (figure 4). This zone, between 0.75 to 2 m, coincides with a sill like structure off the dike

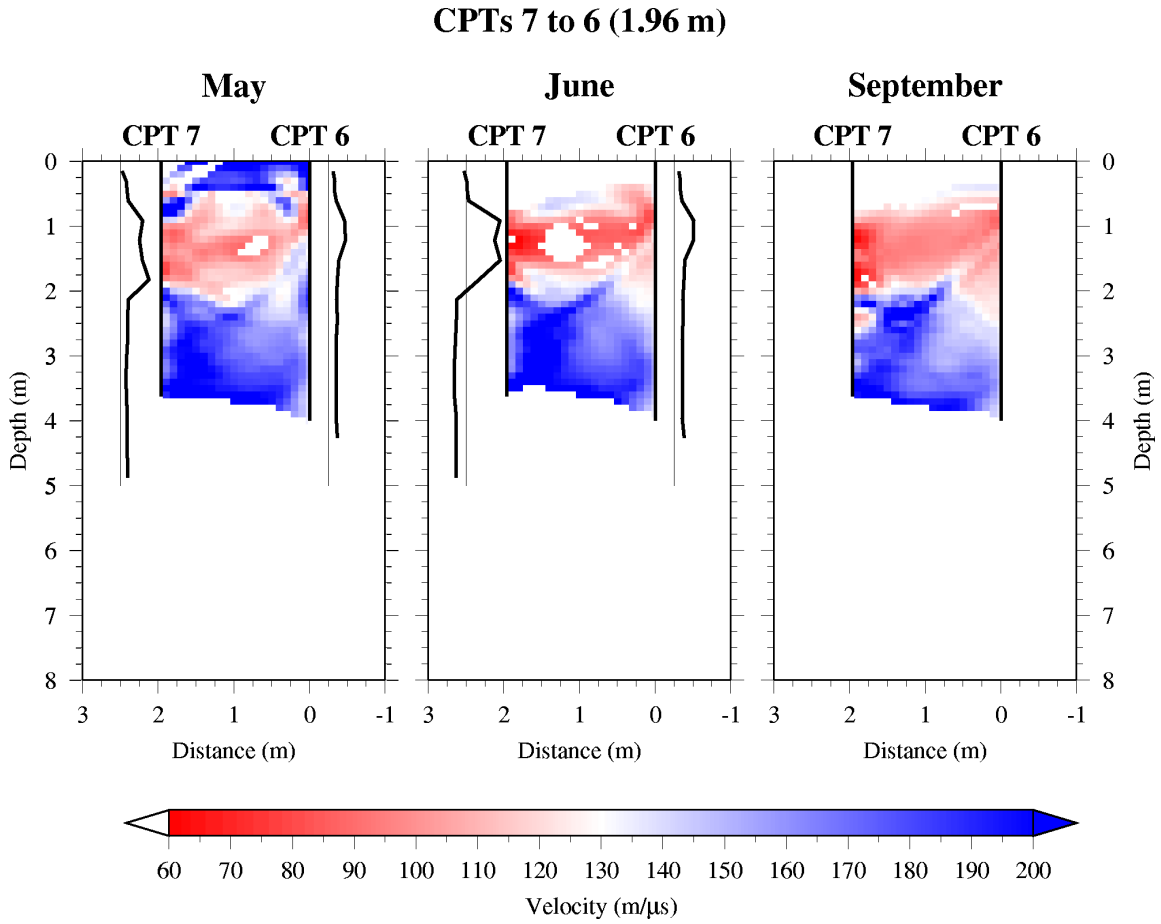

Figure 4. Tomograms from wells CPT 7 - 6. Solid curves to the left and right of the May and June tomogram are the neutron probe soil moisture estimates.

face observed from the trench. In the trench, the sill is 0.5 m to 1.25 m depth. The tomogram indicates that the sill has slower velocity than the surrounding material. The slower velocity suggests that the finer-grained sediments of the sill may retain more water than the surrounding material, causing the velocity anomaly. This slow zone is underlain by higher velocity material even for the initial conditions, indicating that moisture infiltrating the site under natural conditions either is not retained by the coarser grained sediment below the sill, or the water does not penetrate below the overlying sill.

To assess the reliability of the interpretation, plots of ray density indicate where the model has been best sampled (figure 5). The ray density is the total sum of ray lengths through a cell

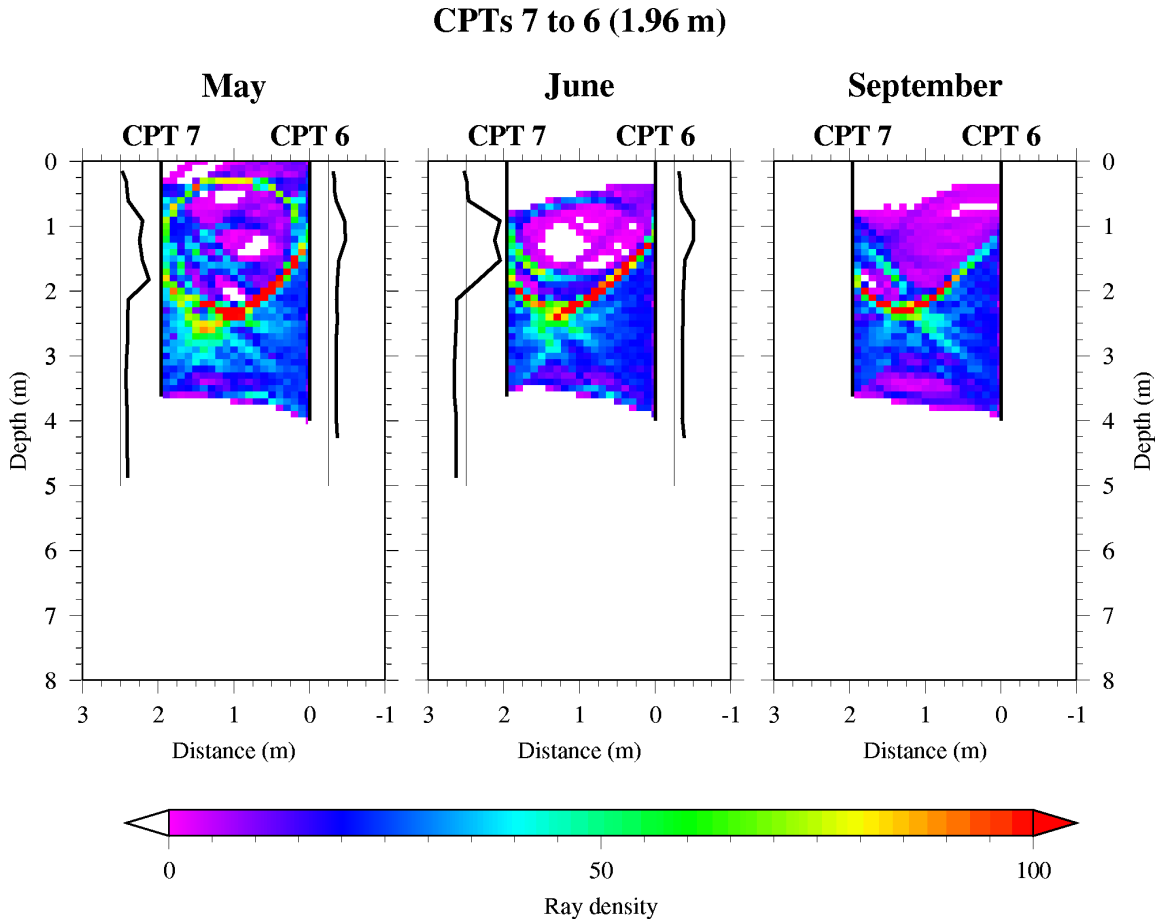

Figure 5. Ray densities from CPT 7 - 6. The ray density is the total length of the raypaths through a cell divided by the length of that cell (0.1 m). Ray densities greater than 100 are plotted in red.

divided by the length of the cell (0.1 m). In the plots, ray density values greater than 100 are plotted in red. Higher ray densities indicate where the model is more reliable. As expected, the ray density is lower in the slow velocity zones. Due to Fermat's principle, rays refract around slow zones. Fermat's principle states that energy takes the path for which the traveltime is a minimum compared with neighboring paths (Sheriff, 2002). Thus, these areas are not as well sampled as the faster, surrounding material. These slow zones may still be interpreted, but the velocity resolution

in these zones is not as good as in the faster zones. The ray density plots indicates that the velocities outside of the slow zone are reliable.

Velocity difference plots show the locations of velocity changes during the infiltration test. In figure 6, the May tomogram is plotted on the left. The two panels at the center and right are the

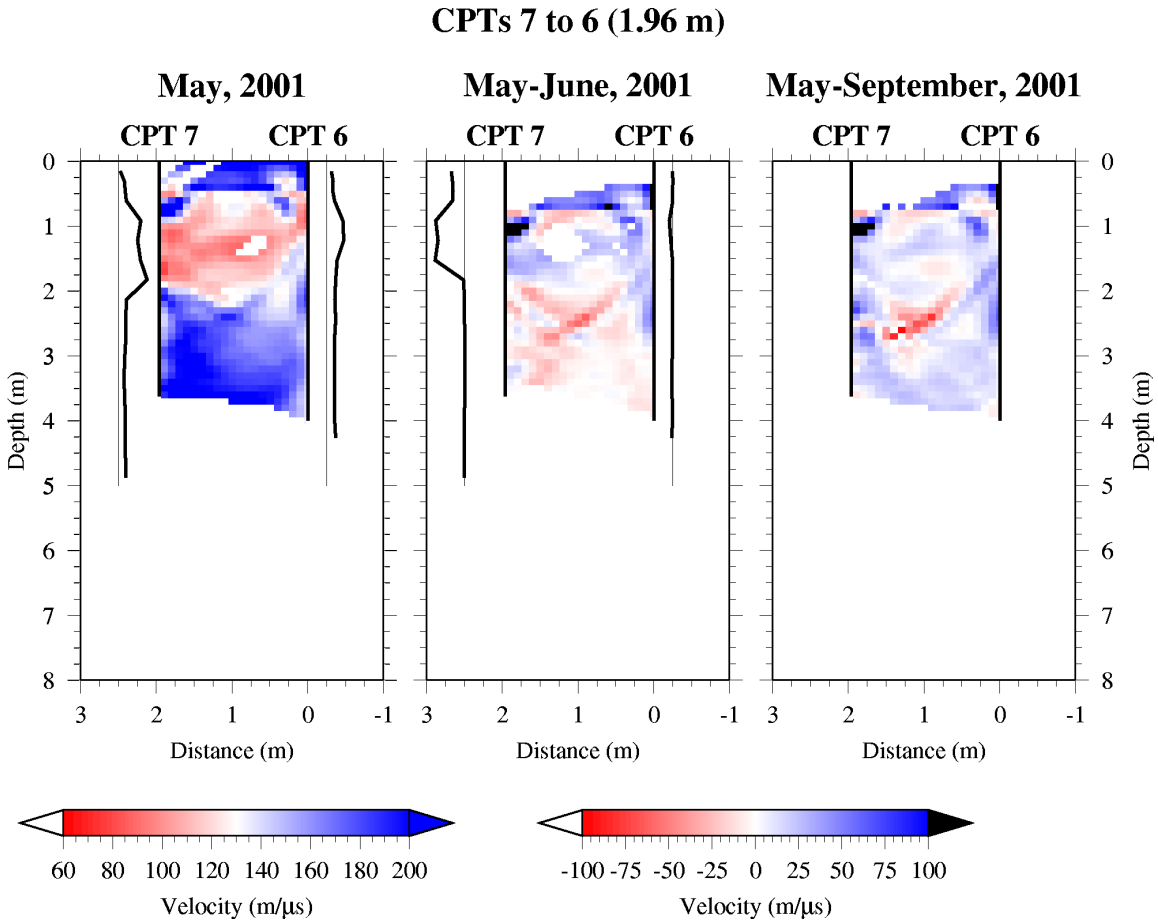

Figure 6. Red velocities in panels 2 and 3 indicate that the velocity has increased since May. Blue velocities indicate a decrease in velocity since May. In the May panel, the neutron-derived soil moisture is plotted as in figures 4 and 5. For the June and September plots, I have plotted the soil moisture *difference* (the soil moisture in May minus the soil moisture in June or September). Thus, an increase in soil moisture will have a negative value (left of the baseline) and a decrease will have a positive value (right of baseline). This convention is followed in all the velocity difference plots.

change in velocity from May. Interestingly, the velocity below about 2 m depth increases slightly in June despite the watering at the surface (figure 6). However, the neutron probe data from CPT 6

and 7 increase slightly, indicating that the observed change in the tomography may be due to noise. By September, the velocity has decreased slightly from the May values.

The tomogram for CPT 3 - 5 (figure 7) indicates a relatively fast layer to about 5.5 m

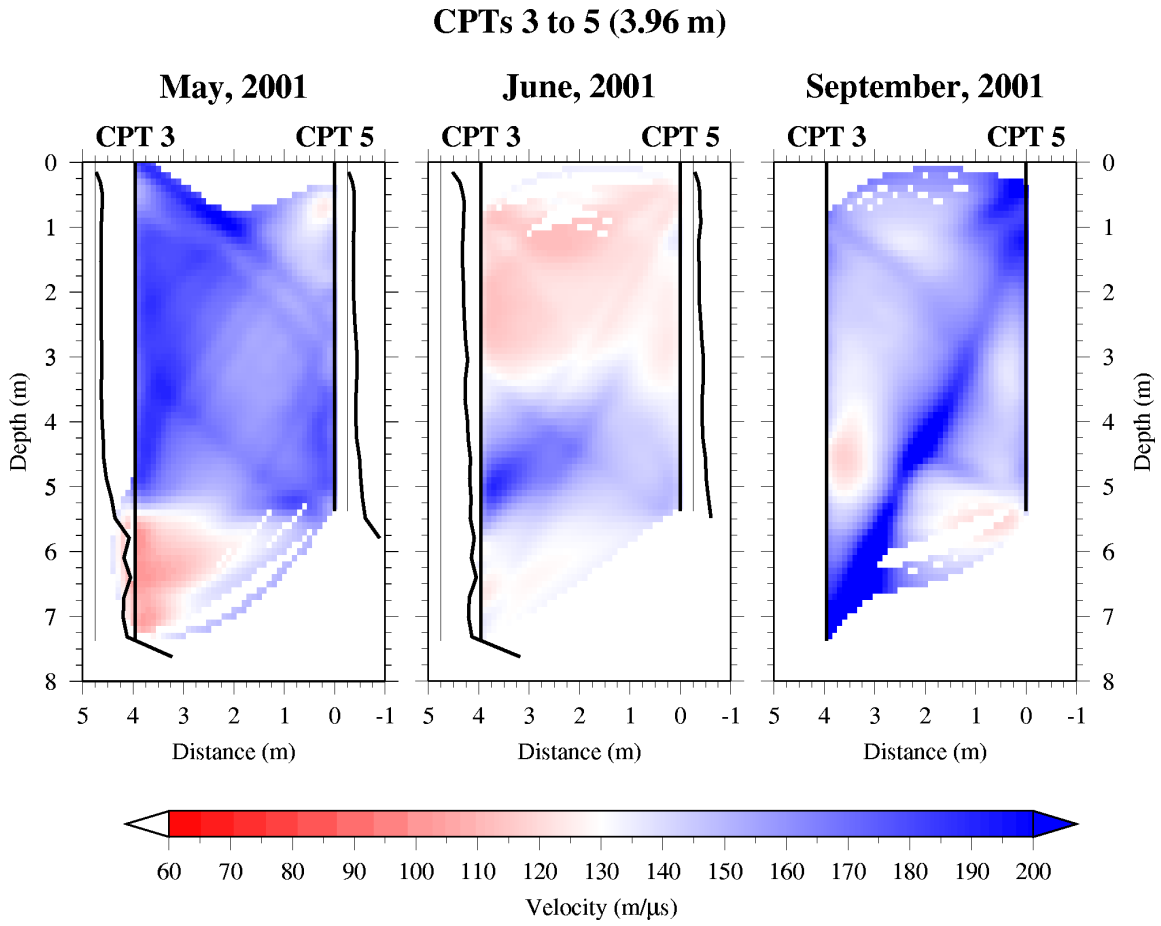

Figure 7. Tomograms from CPT 3 to 5.

depth. A slow velocity zone underlies this layer. The slow zone gradually increases in velocity toward CPT 5; however, this lower zone is not well constrained laterally. The upper portion of the tomogram shows a velocity decrease in the upper 3.5 m in June (panel 2) indicating that water is infiltrating to deeper depths. The slow velocity zone remains below 5.5 m depth. The September panel (panel 3) looks unusual. I think that the data for this experiment may have been incorrectly saved and so the velocities for the September tomogram are unreliable.

In figure 8, the highest ray density values are between 2 to 5 m, indicating that these

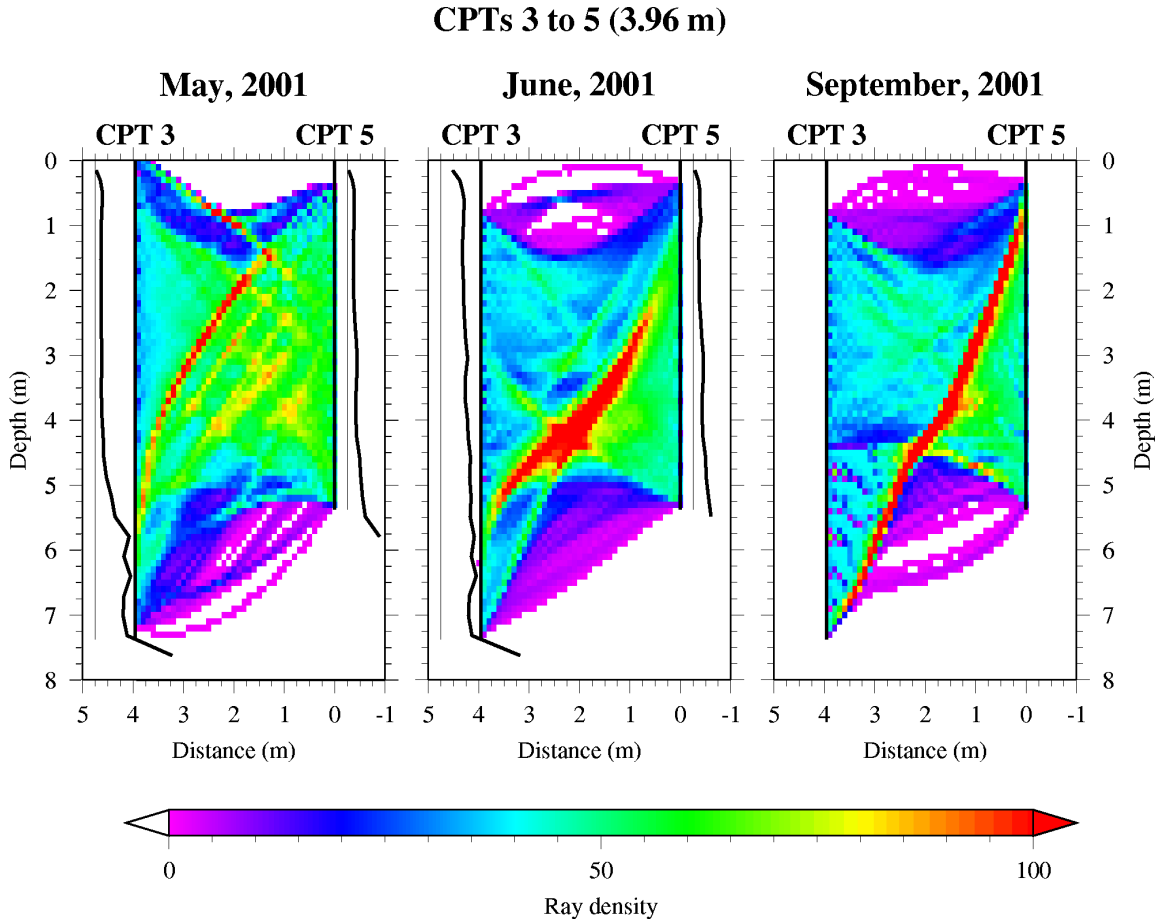

Figure 8. The ray density diagram for CPT 3 - 5.

results are the most reliable. The red stripe from the lower left corner to the upper right corner indicates that the radar energy is focussed along this path. The blue zones at the model's top and bottom show poorer ray coverage. The poorer coverage is due to the acquisition geometry; less redundancy exists at the top and bottom of the model. Results from these regions should be inter-

preted cautiously. The velocity difference figure (figure 9) shows that the velocities decreased

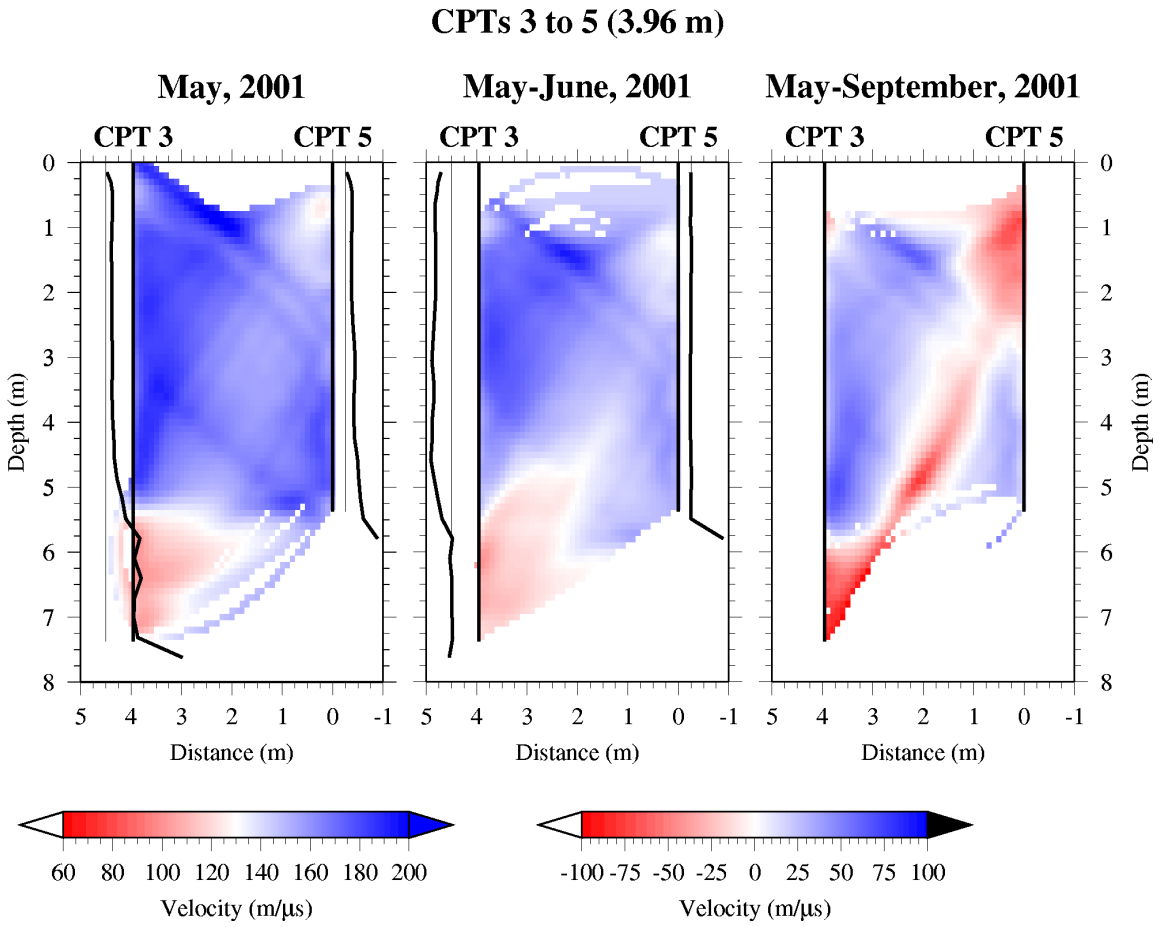

Figure 9. Velocity difference plots for CPT 3 - 5.

between May and June in the upper 4.5 m or so, indicating an increase in the soil moisture content.

The tomogram between CPT 3 - 7 contains the slowest velocities (Table 2) and shows little velocity variation (figure 10). Although not observed, the clastic dike crosses near the center of

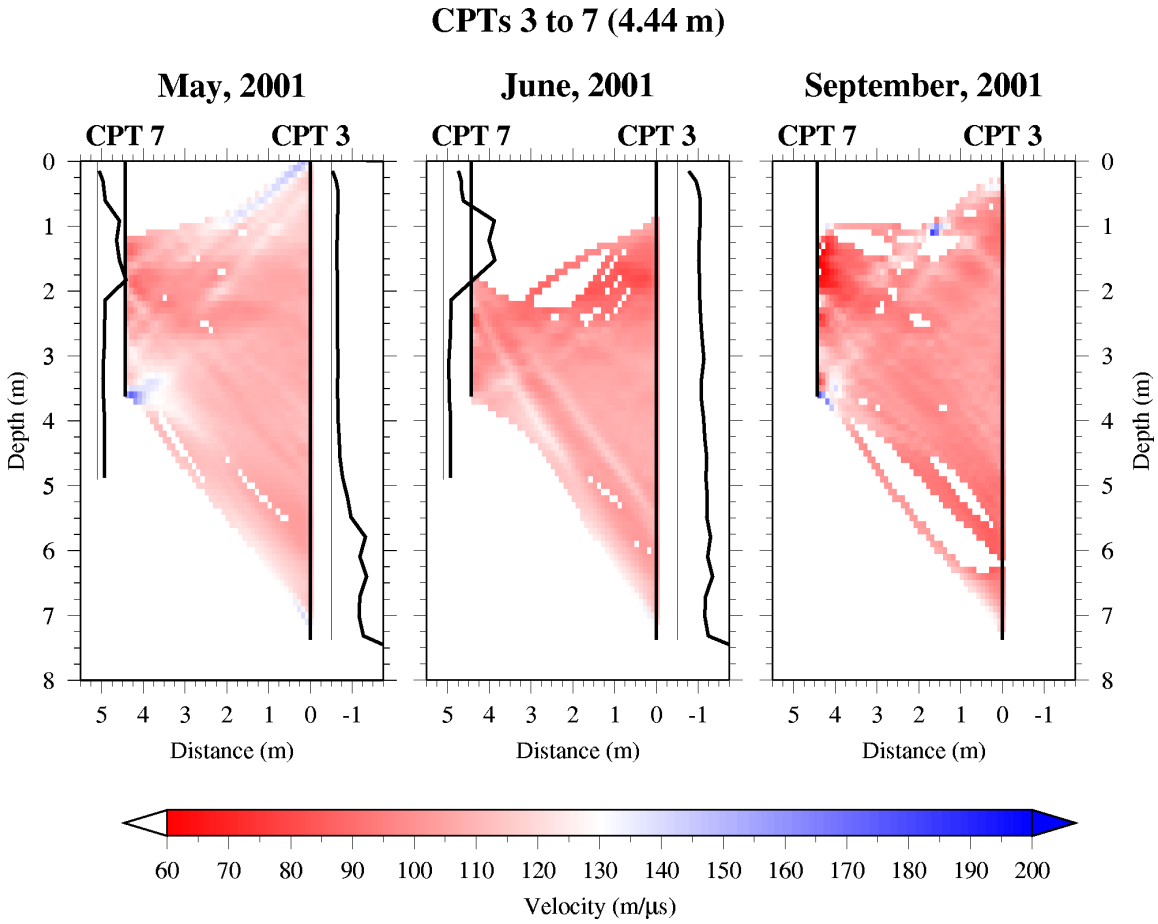

Figure 10. Tomograms from CPT 3 - 7.

the tomogram. A high velocity anomaly is seen at about 3.5 m depth near CPT 7. The higher velocities in the upper right corner near CPT 3 may be an artifact due to the influence of the air.

The ray densities (figure 11) indicate that results near CPT 7 below 2 m are more reliable. The

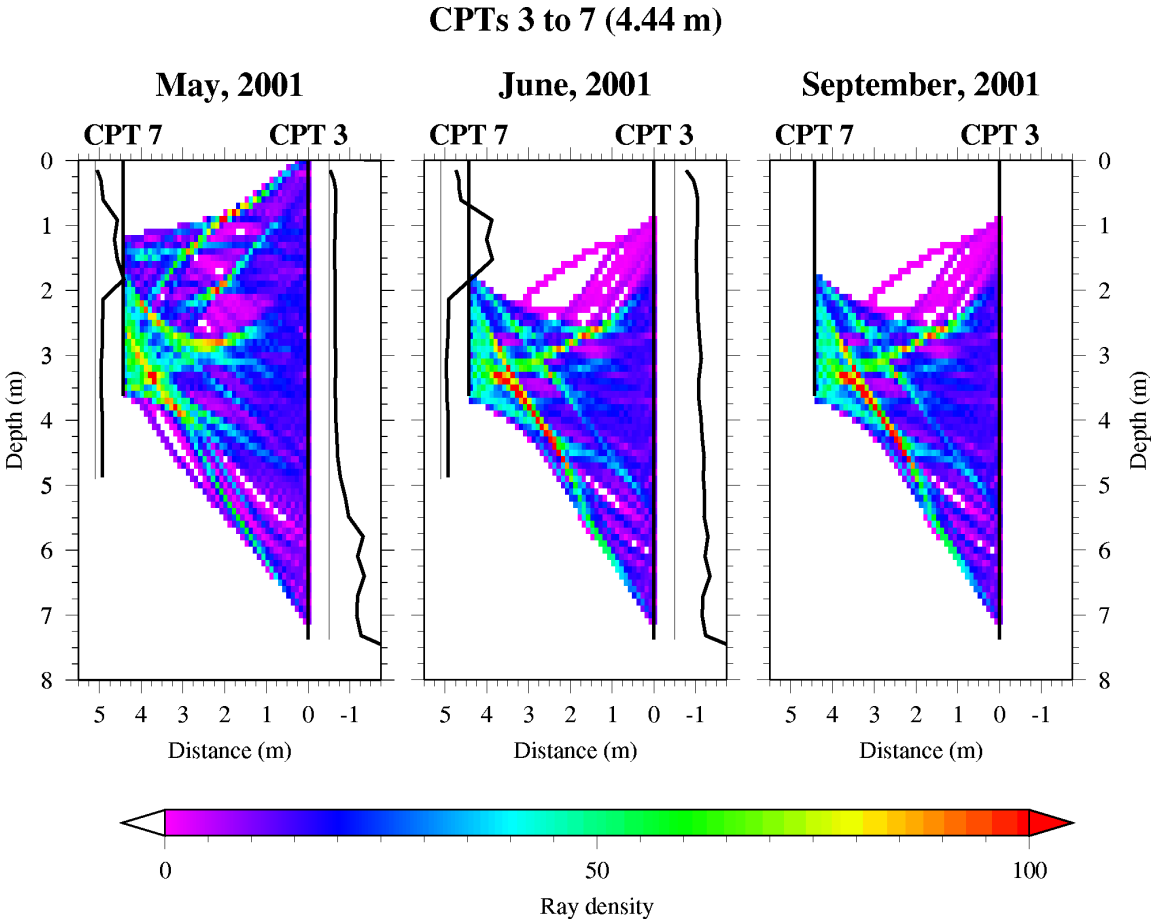

Figure 11. Ray densities from CPT 3 - 7.

velocity difference plot (figure 12) shows that the velocities decreased from May in the June and

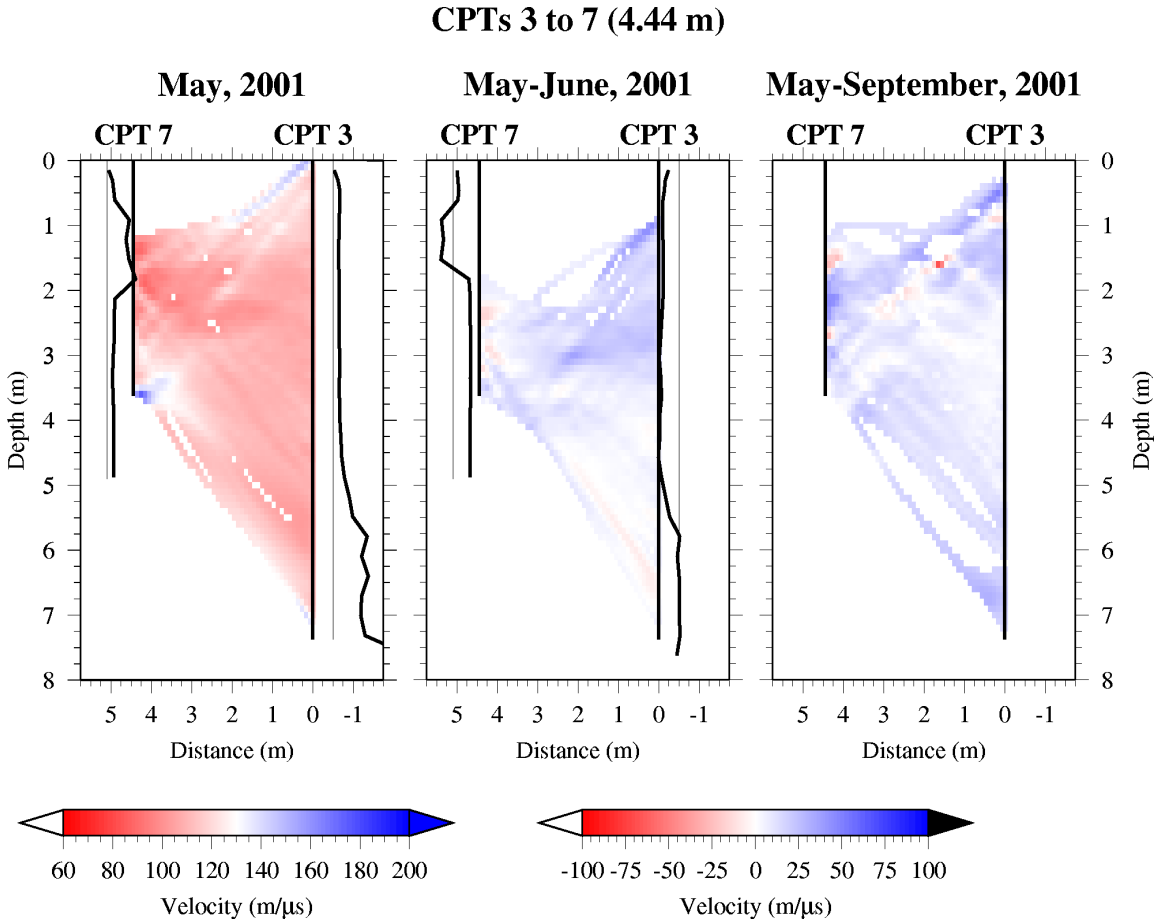

Figure 12. Velocity difference plots from CPT 3 - 7.

September panels. The velocity changes are small and do not appear to correlate with the neutron derived soil moisture content profiles.

The tomogram from CPT 3 - 8 contains a fast zone between about 2 to 5 m (figure 13). A

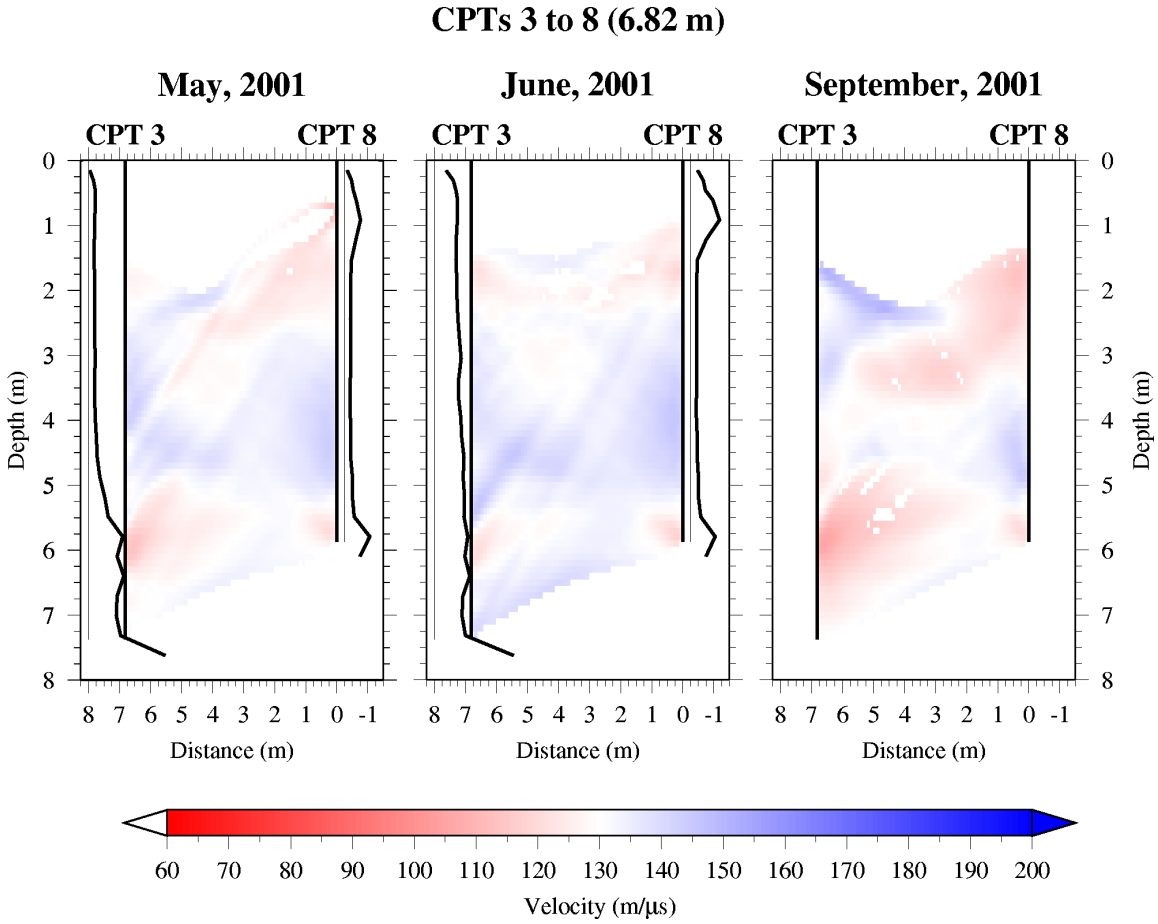

Figure 13. Tomography panels from CPT 3 to 8.

slow zone exists below 5 m. A slow velocity layer may exist above 2 m, but that region is poorly sampled so the zone is not well resolved. This zone, if it exists, may be related to the presence of the sill on the west side of the dike. The slow zone below 5 m depth corresponds well with the neutron derived soil moisture logs. The zone is not continuous between the CPTs, but again this part of the model is poorly resolved. This slow zone increases in velocity in the June panel; the velocity decreases and is more extensive in the September panel. The September panel more clearly shows the slow zones at the top and bottom of the model. The upper zone extends from CPT 8 to about 3.5 m in the center of the tomogram.

The lower zone is more continuous and extends upward to 4.5 m. This tomogram indicates that the water is flowing toward the center of the plane, toward the clastic dike, and the ponding at the approximately 5.0 m level is increasing in thickness.

The ray density plots for CPT 3 - 8 (figure 14) are similar to the ray densities for CPT 3 -

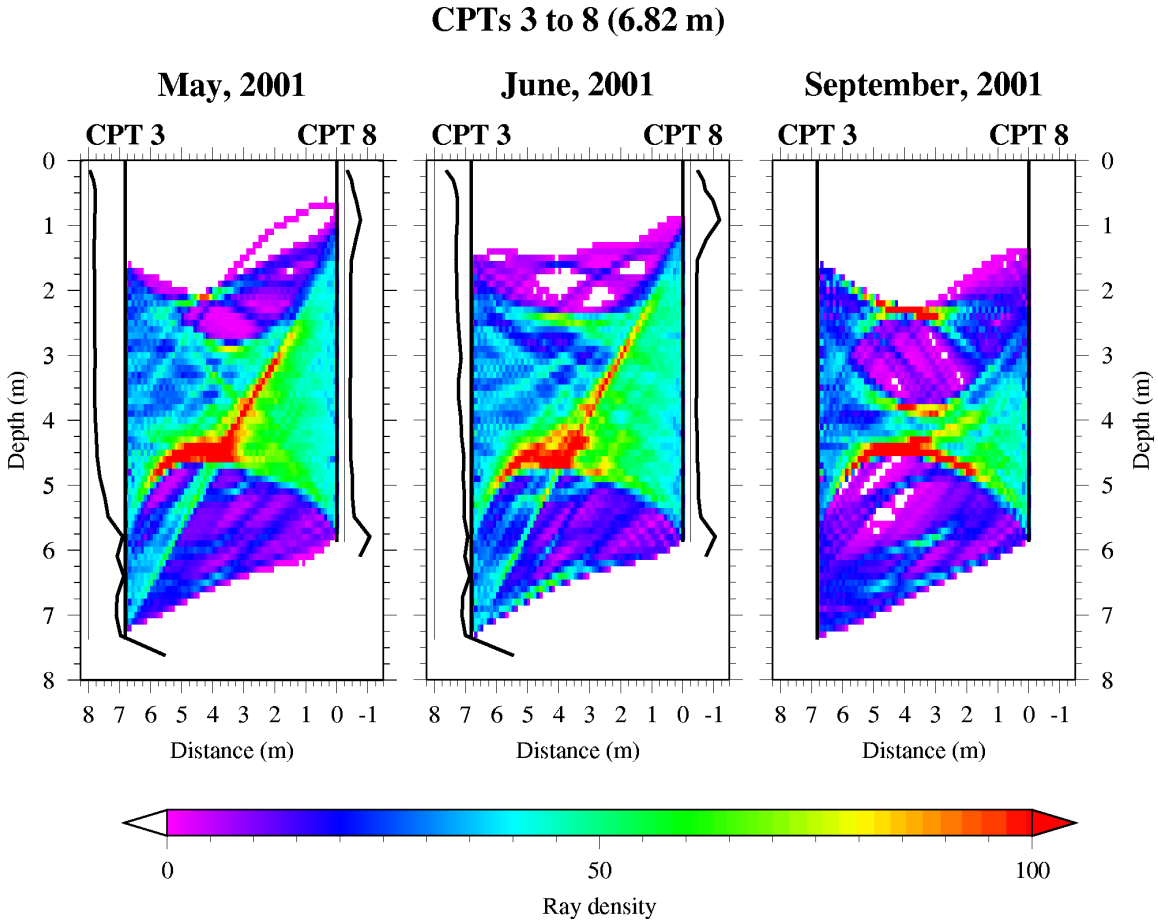

Figure 14. Ray densities from CPT 3 - 8.

5. The most well resolved velocities are near CPT 8 and between 2 to 5 m. The velocity difference

(figure 15) indicates that the velocities increased between May and June, but decreased between May and September.

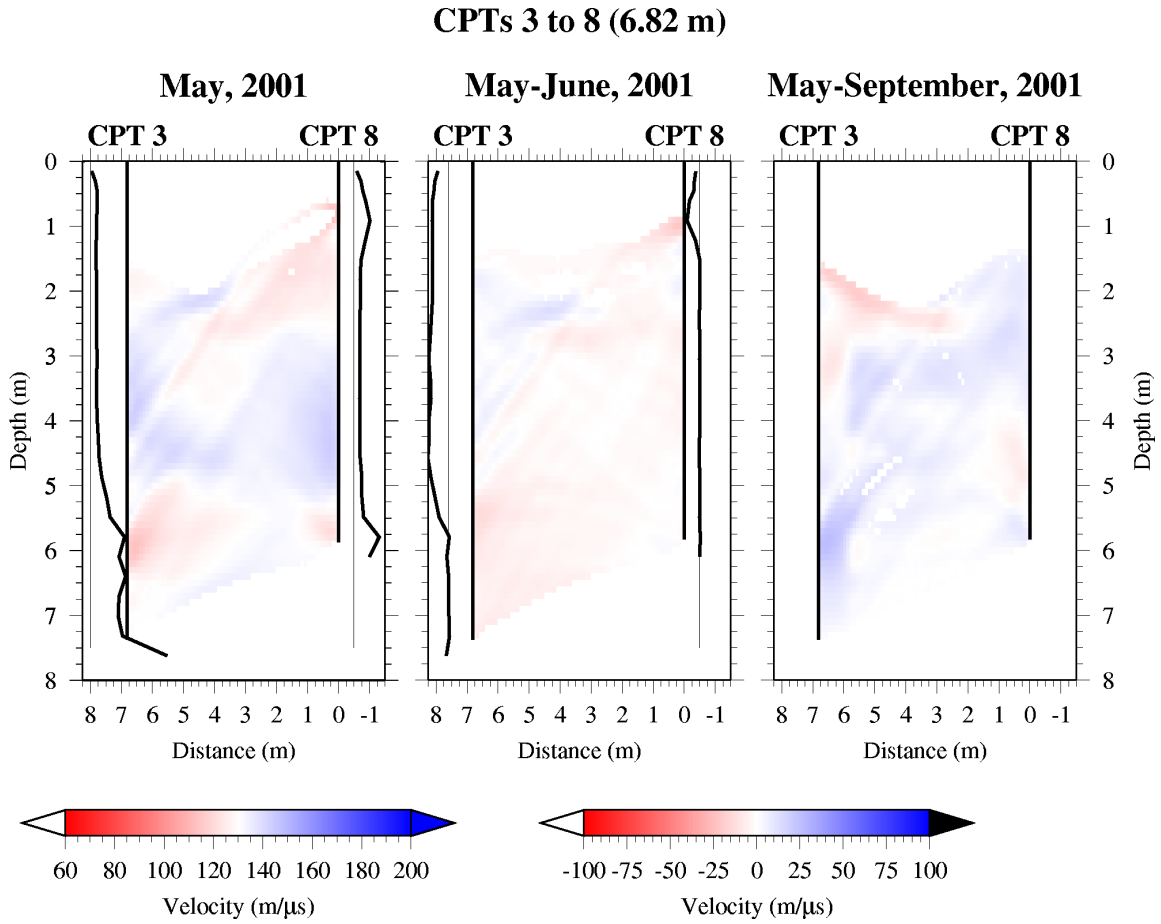

Figure 15. Velocity difference plots for CPT 3 - 8. The base line for CPT 3 changes between panels 1 and 2.

Summary of findings in tomograms

In CPT 3 - 5 and CPT 3 - 8, a slow velocity zone is seen in the tomograms at a depth of about 5.5 m. The neutron log verifies the presence of the zone. The slow zone appears to indicate a change in geology, probably a layer of fine-grained material with higher moisture content.

The upper meter or so of the tomograms is poorly resolved. Poor ray coverage contributes to the poor resolution. However, the closeness of the surface also causes uncertainty. The EM

velocity of air is much faster (0.3 m/ns) than in earth materials. Near the surface, the fastest path will be up the well to the surface, through the air, then down the well again. The effect is most easily seen in the zero-offset profiles (figure 16). Thus, the velocities for the top meter or so of the

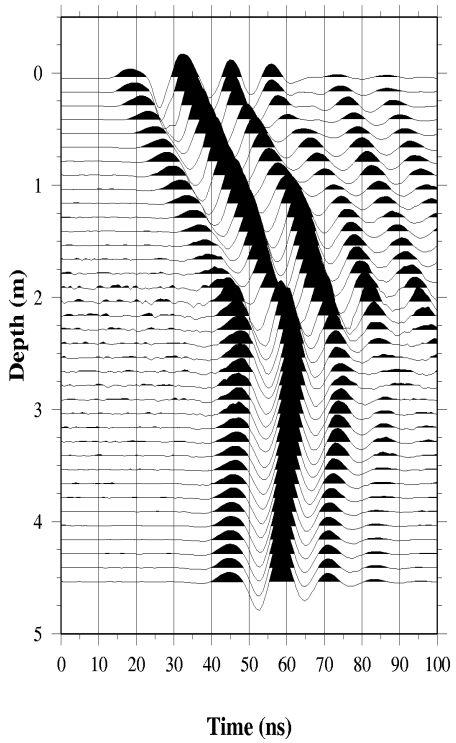

Figure 16. Zero-offset profile between CPT 3 and CPT 5 from the May experiment. Note how the travel time increases from the surface to about 40 ns at 2.75 m depth. The short travel times near the surface show the influence of the fast air velocity.

tomograms are probably not representative of the subsurface, but are a weighted average of the air and subsurface velocity. The effect of water in the pore space is to reduce the sediment velocity. Once the infiltration test starts, the slower subsurface velocity will cause energy from deeper sources to travel through the air, exacerbating the poor resolution in the upper meter or so.

Also, Fermat's principle means that slow velocity zones will be undersampled by the energy. The first arriving energy will preferentially travel through faster zones and avoid slow

zones, biasing the tomograms to faster velocities. Fortunately, large slow zones will be sampled because the path around the slow zone will be too long to compensate for the faster velocity.

At least in the first few days of the infiltration test, water content appears to increase between 0.5 to 2 m depth on the west side of the clastic dike. The presence of the sill may cause this moisture increase. This increase in water will slow the EM velocity through this zone. Again, Fermat's principle would indicate that the energy would avoid these regions, biasing the images toward faster zones. This mis-sampling will be stronger for larger separations between CPTs. Interestingly, CPT 7 and 6 are separated by only 1.96 m and their tomogram has the most detail in the upper few meters.

The clastic dike is not observed in the CPT 3 - 7 and CPT 3 - 8 tomograms, even though these CPTs are on opposite sides of the dike. Tomography, because of the geometry of acquisition, has poor lateral resolution. Instead of imaging the dike, the slower velocity expected from the clastic dike will be smeared horizontally in the tomogram, resulting in a more homogeneous, slower velocity distribution. Interestingly, the tomograms that cross the dike, CPT 3 - 7 and CPT 3 - 8, have the slowest average velocities. The slower average velocities may further indicate that the dike has a slower velocity that the surrounding material. Also, CPT 3 - 7 is the most homogeneous of the tomograms. The slower velocity could occur because the energy travels diagonally across the dike, thus traveling longer in the dike compared to the CPT 3 - 8 tomogram. These two tomograms, compared to the two that do not cross the dike, indicate that the dike has a slower velocity and retains water better than the surrounding material. This conclusion is verified by moisture measurements made in the dike during the excavation.

Comparison with neutron probe data

The neutron probe uses a radioactive source to measure the presence of hydrogen atoms in the ground. The number of neutron counts is related to the amount of hydrogen atoms in the ground. The most common source for hydrogen atoms in the ground is water. So, the neutron probe results are usually interpreted in terms of porosity or soil moisture content (Rider, 1996). The neutron probe data were acquired on seven days between May 30, 2001 to June 29, 2001 (Table 3).

Table 3: Neutron probe acquisition dates

Date	Method
May 30, 2001	Neutron probe
June 6, 2001	Neutron probe
June 11, 2001	Neutron probe
June 14, 2001	GPR and Neutron probe
June 18, 2001	Neutron probe
June 21, 2001	Neutron probe
June 29, 2001	Neutron probe

The neutron probe data show similar features (figure 17). This behavior is evident in the

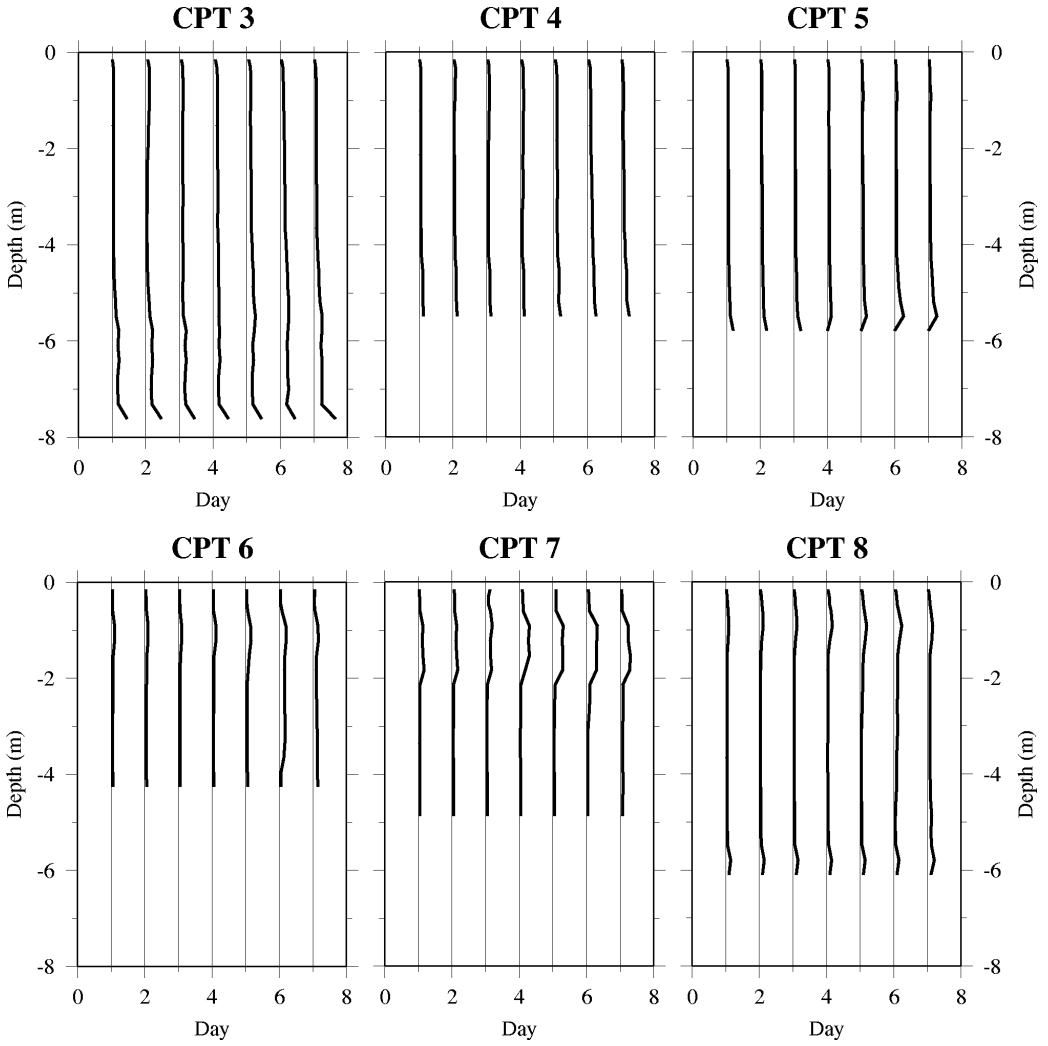

Figure 17. Soil moisture estimates derived from neutron probe measurements at wells CPT 3 to CPT 8. See table 3 for sampling days. In CPT 3, the ground is drying above 4 m between day 4 (June, 14, 2001) to day 7 (June 29, 2001). In CPTs 6 to 8, the west side of the dike, a zone between about 0.5 to 2.0 m shows increasing then decreasing soil moisture content.

data from CPT 3 (figure 17). The water appears to pond between about 5.5 to 7.5 m depth. Over the duration of the measurement times, the ponded water appears to thicken toward the surface. In other words, the water can not flow below about 7.5 or greater, so the water accumulates above this level. Throughout the sampled volume, the moisture content increases when the high moisture zone at about 0.5 to 2 m penetrates into the deeper sediments. CPT 3 and CPT 8 indicate that

the section is drying by the end of the experiment as the soil moisture values are decreasing in the June 29, 2001 measurements.

CPT 3 and CPT 7 are within the infiltrated region. The neutron probe data from these CPTs indicate that the moisture content increases at 0.5 to 2 m depth. In CPT 3, the underlying sediment's soil moisture content increases from around 4 percent before the test to between 10 to 25 percent after June 11. This soil moisture increase probably indicates the passage of the moisture front. In CPT 7, the water content increases between 0.5 to 2 m from May 30 to June 14, then stays at about the same for the rest of the experiment.

Outside the infiltration region, CPT 6 shows a similar soil moisture changes to CPT 7, but the water starts to infiltrate deeper by June 21, 2001. Once the water penetrates below the 0.5 to 2 m level, the soil moisture throughout the section increases from around 5 percent to 11 percent. CPT 4 has similar behavior to CPT 3, an early breakthrough with increasing moisture content in the underlying section. CPT 5 shows a small amount of soil moisture increase around 1 m. Near the end of the experiment, the soil moisture increases greatly at about 4.5 m from 7 to 8 percent to 11 to 16 percent by June 21, 2001. This deep increase, without an obvious decrease in water content in the 0.5 to 2.0 m zone, may indicate that water is flowing laterally at around 5 m depth.

The sill on the west side of the clastic dike probably causes the moisture increase at 0.5 to 2.0 m depth. The fine-grained sediments in the sill do not allow the water to descend into the coarser-grained sediments below. The water content increases in the sill until the water entry pressure of the underlying layer is reached and the water infiltrates into these sediments (A. Ward, pers. communication).

The radar velocity can be converted to dielectric constant using:

$$\kappa = \frac{c^2}{v^2} \tag{4}$$

where c is the EM velocity in air (0.3 m/ns). To convert the dielectric constant to soil moisture content, I used Topp's equation, an empirically determined relationship (Topp et al., 1980):

$$\theta = -5.3\times10^{-2} + 2.92\times10^{-2}\kappa - 5.5\times10^{-4}\kappa^2 + 4.3\times10^{-6}\kappa^3 \tag{5}$$

where θ is the water content and κ is the dielectric constant. This relationship may not match the true relationship for the infiltration site.

I have converted the velocities in the tomograms to soil moisture plots. Again, these plots have the same color scale to ease comparison. In these plots red indicates low moisture content (fast velocity) whereas blue indicates high moisture content (slow velocity). As expected, the soil

moisture content plot for CPT 7 - 6 (figure 18) shows high moisture in the region between 1 to 2

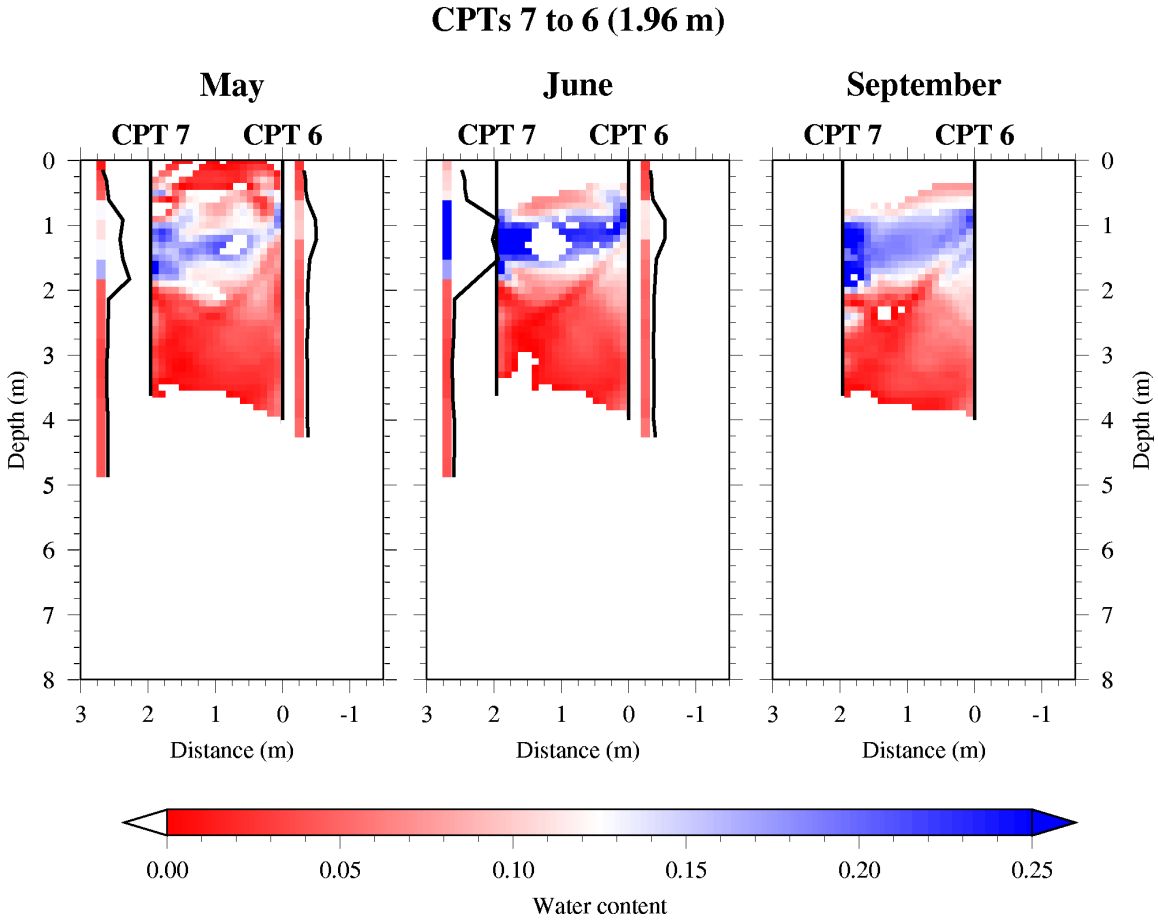

Figure 18. Soil moisture content from CPT 7 to 6. The soil moisture content derived from the neutron probes is also plotted in the figure. I have also color coded the neutron soil moisture using the same color scale in the water content plots.

m depth. The percent of soil moisture matches well with the neutron derived values. The soil

moisture values from CPT 3 - 5 (figure 19) also match the neutron derived soil moisture values,

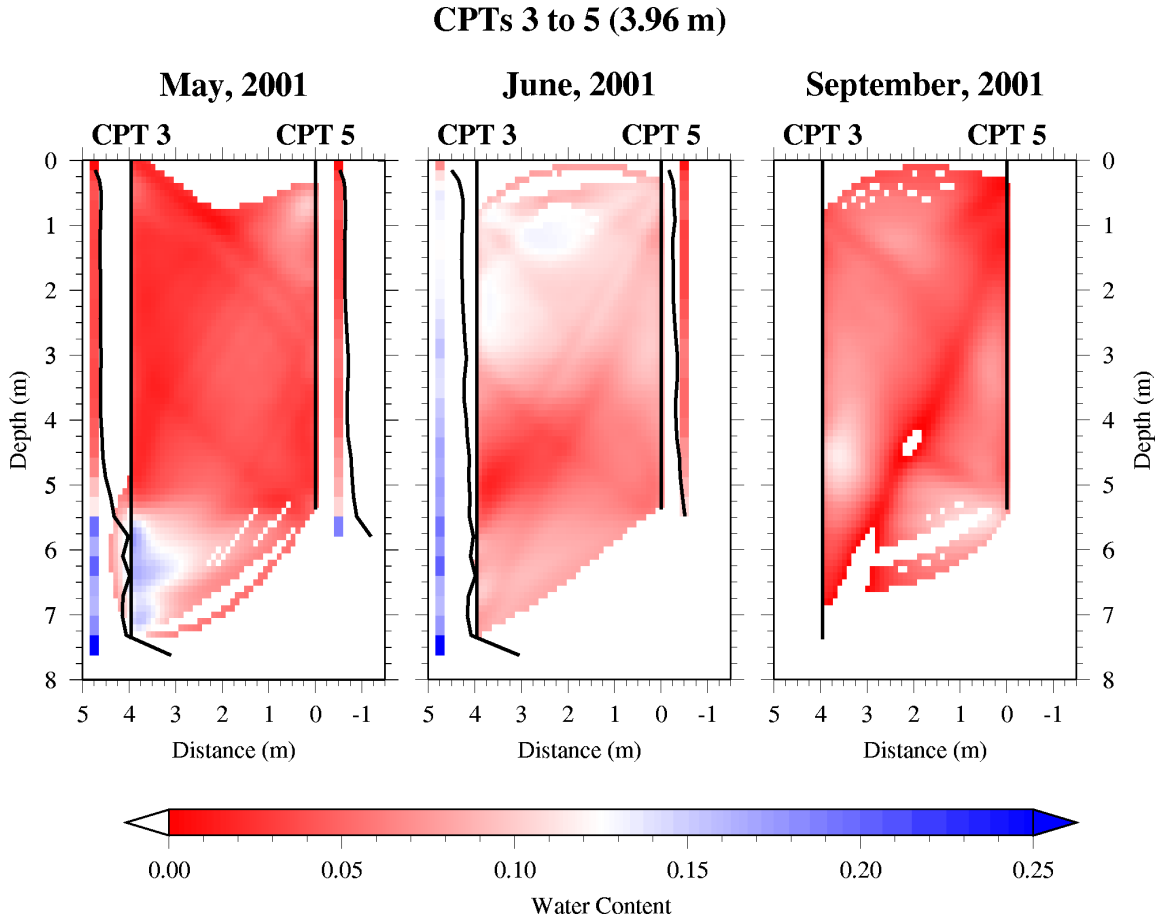

Figure 19. Soil moisture content for CPT 3 - 5.

especially in CPT 3 in May. The June CPT 3 values are somewhat higher than the tomography-derived results, but the June plot shows a upward increase in soil moisture content even though the magnitudes are less. This magnitude difference could be due to the different sampling volumes of

the methods. For CPT 3 - 7 (figure 20), the match is not as strong. The soil moisture content for

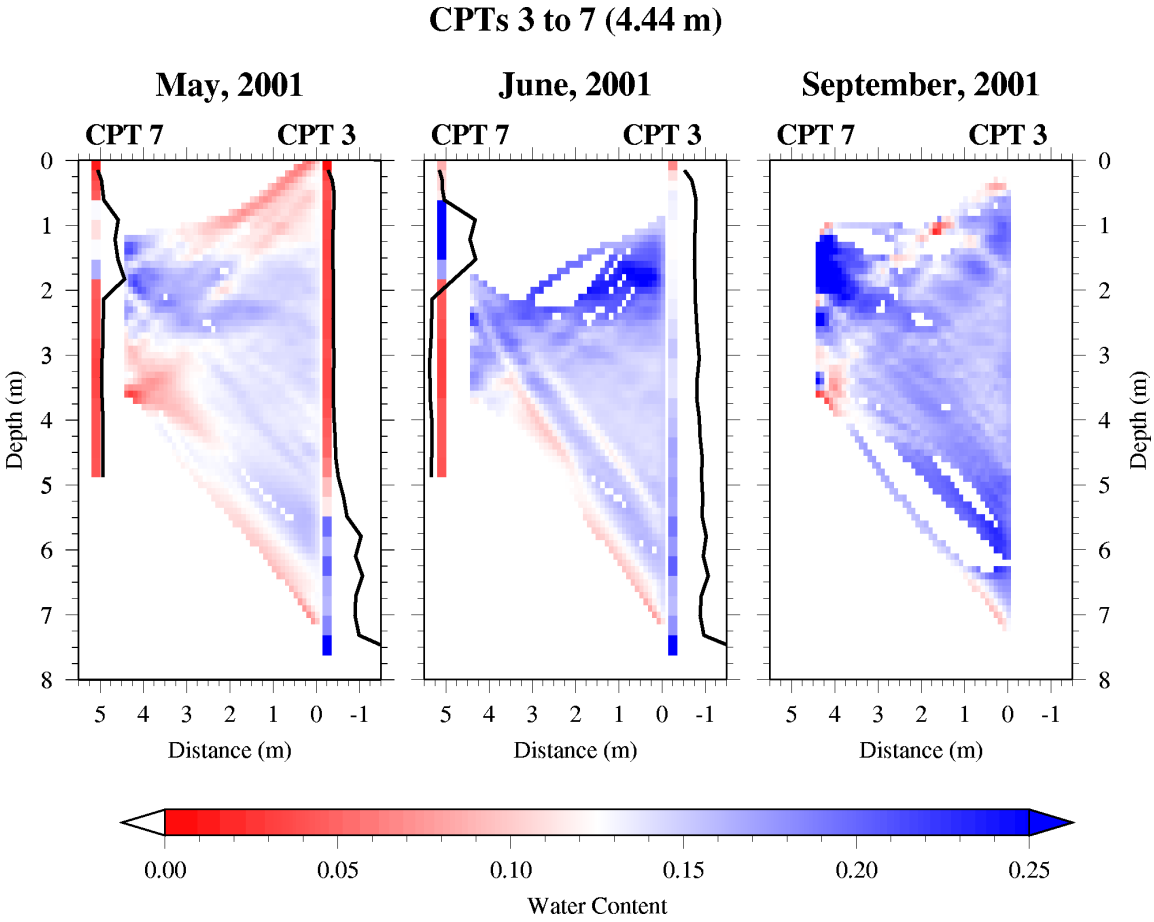

Figure 20. Soil moisture content values for CPT 3 to 7.

CPT 3 - 8 is relatively constant (figure 21). Near the base of the CPTs, the moisture content

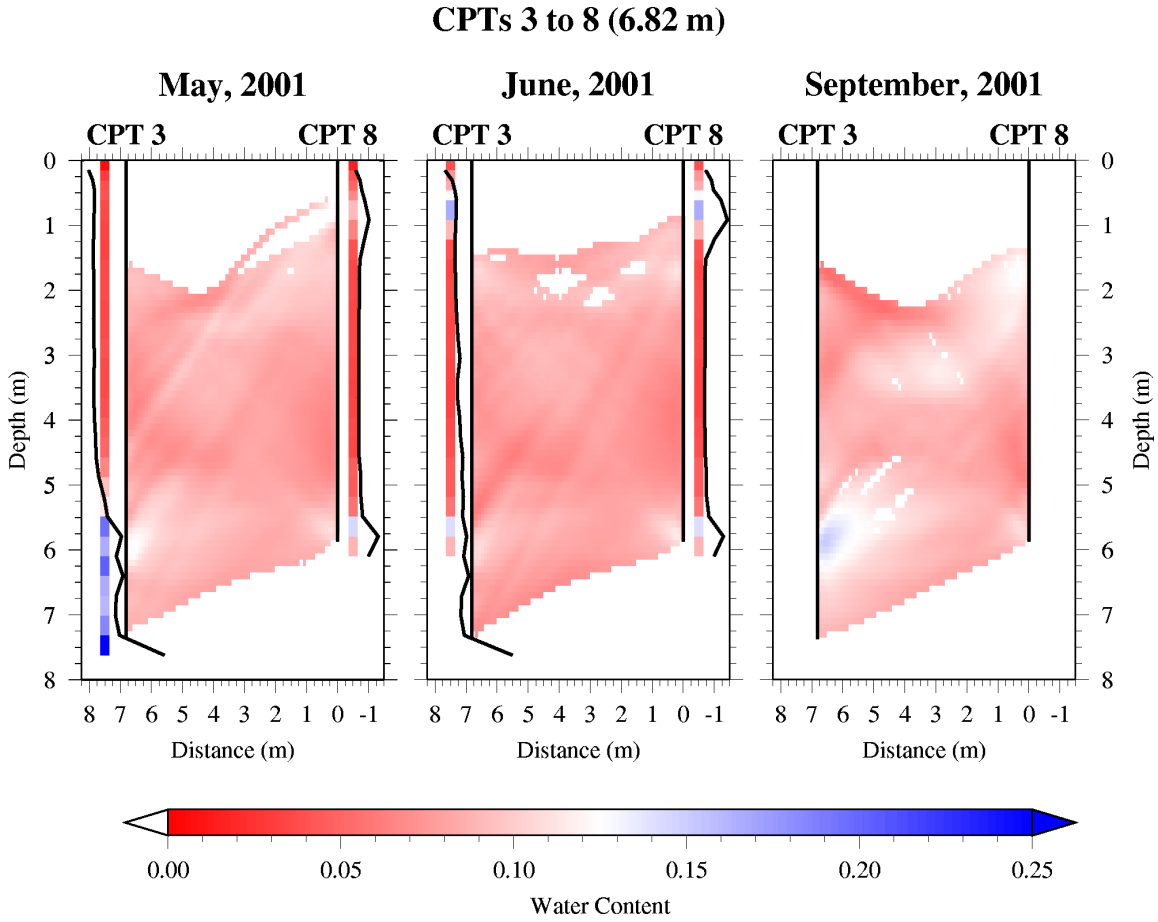

Figure 21. Soil moisture values for CPT 3 to 8.

increases in the velocity derived soil moisture content plots, but not as much as the neutron derived soil moisture content.

I can convert the soil moisture content to dielectric constant, using Topp's equation in another form (Topp et al., 1980):

$$\kappa = 3.03 + 9.3\theta + 146.0\theta^2 - 76.7\theta^3 . \quad (6)$$

From the dielectric constant, velocity is easily computed (see equation 4):

$$v = \frac{c}{\sqrt{\kappa}}. \tag{7}$$

To directly compare the tomogram and the neutron probe results, I compare 1-D velocities based on the tomograms with velocities derived from neutron probe (figure 22). To compute the 1-

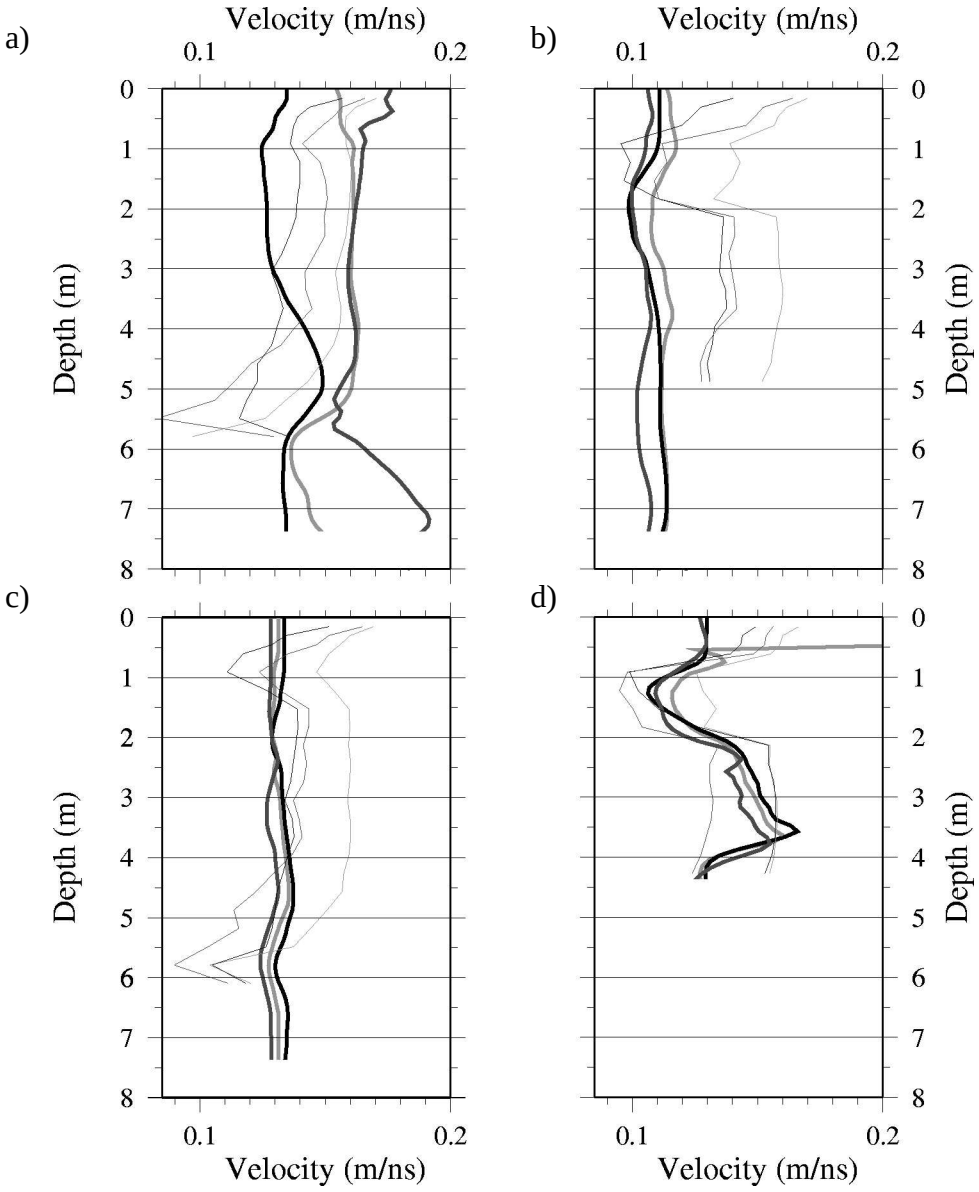

Figure 22. Comparisons of velocities from 1-D tomograms and average velocity of the two wells based on the neutron probe data. Neutron probe soil moisture values converted to velocities using Topp's equation. a) CPT 3 - 5; b) CPT 3 - 7; c) CPT 3 - 8; d) CPT 7 - 6. Thick lines are the 1-D tomogram, thin lines are the average neutron-derived velocity from the two relevant CPTs. May is the light grey line, June is the black line, and September is the dark grey line.

D velocities from the tomograms, I average the velocity across each layer in the model. For the neutron probe data, I converted the soil moisture values to velocities using Topp's equation and then averaged the values from the two relevant wells. In general, the neutron probe measurements show more variation in water content than the 1-D velocities. The exception is for the CPT 7 - 6 tomogram. The shape of the curves and the relative velocity changes are similar (figure 22d). Not surprisingly, the CPT 7 - 6 tomogram also has the most interesting and consistent velocity structure (figure 5 and 6) over the infiltration test.

An important consideration when comparing results from different methods is the sampling volume of each measurement. For the radar data, the sampling volume (wavelength) is about 1.8 m. For the neutron probe, the sphere of influence is about 0.2 m in radius (Rider, 1996). The values from the radar data are averaged over a larger volume, so small scale changes will not be observed.

Reliability Issues

The largest error in the tomograms is due to the deviation in the CPTs. I have assumed in the tomographic analysis that the CPTs are vertical. I have used this assumption, even though I know the wells are deviated, because no measurements of the deviation exist. The incorrect locations of the source and receiver due to CPT deviation will cause incorrect estimations of the velocities. However, velocity difference plots should more accurately measure the relative velocity changes in the subsurface.

When calculating the differences between different days, the experimental design should be the same. Unfortunately, many changes to the site occurred between May and September. Between the May and June tomography experiments, the equipment for the infiltration test was installed. To more accurately control the amount of water applied during the test, a tent was con-

structed over the test area. At CPT 3 and CPT 7, the height of the tent was so low that the antennas could not be placed for proper calibration. The low ceiling made holding the antennas vertically difficult, perhaps causing an inaccurate measurement of the origin time of the transmitted pulse. An inaccurate origin time will cause the resulting velocities to be shifted by a constant amount and that amount will vary between the different acquisition days. The relative velocity changes within the individual tomograms are still interpretable as changes, but the magnitudes will be wrong. This problem has similar effects in the interpretation of the velocity difference plots.

Also, I switched the location of the transmitter and receiver for the CPT 3 - 5 tomography acquisition. In May, the transmitter was in CPT 3 and the receiver was in CPT 5. For the June and September experiments, the transmitter was in CPT 5 and the receiver was in CPT 3. Even though the antennas were switched, the energy paths between the transmitter and the receiver should be identical by reciprocity. Of the three CPT 3 - 5 tomograms, the September tomogram is the most anomalous. If reciprocity were violated, the May tomogram should have been anomalous.

I can compensate for the removal of the top of the CPT casings between the May and June experiments. However, if the stated length of casing removed is wrong, the locations of the transmitter and receiver for May will be incorrect compared to June and September. The effects of this mislocation will probably be strongest in the velocity difference plots.

Trenching the dike caused another major change to the site. When the September experiment was conducted, the ground around CPT 1 and CPT 2 had been removed, exposing about 3 m of their PVC casing. These CPTs could not be reoccupied for tomography. The trench edge was about 1 m or less from CPTs 3 and 8. As I mentioned earlier, the EM velocity of air is fast compared to sediments, especially wet sediments. Some of the recorded energy in September may have traveled along the vertical trench surface through the air, as described in the early discussion

of surface effects. Although evidence of this out-of-plane propagation is not obvious, such events may be in the data and effect the results.

To accurately image the clastic dike or other vertical structures, antennas must be located along the surface between the CPTs. These additional data will more accurately image the horizontal velocity changes in the ground. Although horizontal resolution still will be less than the vertical resolution, antennas along a third side will improve the horizontal resolution significantly. Additionally, incorporating model constraints, such as the location of the dike, into the inversion may further improve the resolution and reliability of the tomography experiment.

Conclusions

GPR has great potential to observe changes in subsurface soil moisture content over time. The tomography data images changes in the subsurface velocity between May and September. The tomogram from CPT 7 - 6 images a slow velocity zone about 1 to 2 m in depth that correlates with high soil moisture content. Although quantitative soil moisture content estimates are not presented, in some cases the tomography data show relative changes in soil moisture content. The presented results are promising. Tomography will probably be even more effective at determining velocity changes at deeper depths in the subsurface, away from the effects of fast air velocities at the surface.

Unfortunately, the design of the infiltration test may have limited the reliability of the tomography interpretation. The CPTs were more shallow than originally planned. A further complication is that the investigation seeks to measure changes in water content. The presence of water reduces the EM velocity, causing first arriving energy to avoid such zones. Also, the target is close to the surface, increasing the likelihood that the first arriving energy will travel through the air at the surface instead of through the slow velocity target zone. With more care in designing

the geophysical experiment within the context of the infiltration test, good results about the moisture distribution in the subsurface are possible.

References

Aldridge, D. F., and D. W. Oldenburg, Two-dimensional tomographic inversion with finite-difference traveltimes, Journal of Seismic Exploration, 2, 257-274, 1993.

Alumbaugh, D., P. Y. Chang, L. Paprocki, J. R. Brainard, R. J. Glass, and C. Z. Rautman, Estimating moisture contents in the vadose zone using cross-borehole ground penetrating radar: A study of accuracy and repeatability, Water Resources Research, 38, 1309, doi:10.1029/2001/WR000754, 2002.

Binley, A., P. Winship, R. Middleton, M. Pokar, and J. West, High-resolution characterization of vadose zone dynamics using cross-borehole radar, Water Resources Research, 37, 2639-2652, 2001.

Fayer, M. J., C. J. Murray, D. G. Horton, and A. L. Ward, Influence of Clastic Dikes on Vertical Migration of Contaminants in the Vadose Zone: FY 2001 Test Plan, Pacific Northwest National Laboratory, 2001.

Menke, W., Geophysical Data Analysis: Discrete Inverse Theory, Academic Press, Inc., pp. 289, 1989.

Murray, C. J. and M. J. Fayer, Influence of Clastic Dikes on Vertical Migration of Contaminants in the Vadose Zone, Pacific Northwest National Laboratory, 2001.

Paige, C. and M. Saunders, LSQR: An algorithm for sparse linear equations and sparse least squares, Assn. Comp. Math. Transactions on Mathematical Software, 8, 43-71, 1982.

Rider, M., The Geologic Interpretation of Well Logs, Whittles Publishing, Caithness, UK, 280 p., 1996.

Sheriff, R. E., Encyclopedic Dictionary of Applied Geophysics, Society of Explorations Geophysicists, Tulsa, OK, 429 p., 2002.

Topp, G. C., J. L. Davis, and A. P. Annan, Electromagnetic determination of soil water content: Measurements in coaxial transmission lines, Water Resources Research, 16, 574-582, 1980.